universität wien

MASTERARBEIT | MASTER'S THESIS

Titel | Title

Combining DNA-PAINT with iSCAT: Towards Super-Resolution Imaging Based on Elastic Scattering

verfasst von | submitted by

Emanuel Traiger B.Sc.

angestrebter akademischer Grad | in partial fulfilment of the requirements for the degree of

Master of Science (MSc)

Wien | Vienna, 2025

Studienkennzahl lt. Studienblatt | Degree programme code as it appears on the student record sheet:	UA 066 876
Studienrichtung lt. Studienblatt | Degree programme as it appears on the student record sheet:	Masterstudium Physics
Betreut von | Supervisor:	Univ.-Prof. Dipl.-Ing. Dr. Thomas Juffmann

Contents

Acknowledgments

First and foremost, I would like to thank Prof. Thomas Juffmann for his continuous support and guidance throughout my thesis and the opportunity to work in his lab. I deeply appreciated his willingness to take the time to discuss problems with me — even joining me in the lab when needed. These moments helped me grow not only scientifically, but also in the way I approach challenges with more professionalism and structure. His calm and thoughtful manner made it a real privilege to work with him.
I also want to thank Dr. Francisco Balzarotti for his interest in and valuable input on my work, and for the insightful discussions we had during our collaboration.
I am sincerely grateful to my supervisor Ilia, whose warm and calm presence, combined with sharp scientific insight, made working on this thesis an incredibly supportive experience. I always felt I could rely on him.
A big thank you goes to Alessandro — working with him was not only extremely instructive but also genuinely fun. His support both in the lab and beyond (especially in the ADC theater group) made this time especially memorable. I truly could not have destroyed the magic plasmid without him.
To Barbara, who shared the desk and built the setup with me during the first half of this journey: I am grateful not only for our collaboration but also for the friendship that developed. When she left the group, something really changed — and I missed her a lot.
Oliver — thank you for your dedication and teamwork during the overlapping phase of our projects. Without you, many things would have been a lot more difficult. I also really enjoyed working with Ipek, whose motivation, helpfulness, and care brought great energy to the lab.
Clara, your help — even after finishing your PhD — meant so much to me. Thank you for being so generous with your time and apologies for suspecting you are evil. Florian, thank you for always being pragmatic and helpful when I needed it.
To Maximilian, it was a pleasure to work with you on our joint experiments. To Emma, I owe special thanks for your help with the DLS measurements — you saved me a huge amount of work!
Finally, I want to thank Hanieh, Ivana, Raphael, Dante, Martino, Sami, Tilman, Luis, Philipp, Victoria, and Zdenek — for all the little (and not so little) ways in which you contributed to a great working atmosphere. It was a pleasure to share this time with you.

Abstract

Light microscopy remains one of the most important tools for studying the microscopic world. As the samples we want to investigate become smaller and the processes faster, and as experimental environments become increasingly complex, microscopy techniques must adapt accordingly. This thesis explores the combination of the super-resolution microscopy technique DNA-PAINT with the highly sensitive interferometric scattering (iSCAT) technique by employing elastically scattering gold nanoparticles (GNPs) with a diameter of 20 nm as labels.
We hypothesize that this combination provides several advantages: GNPs are less sensitive to environmental influences than many fluorescent labels, do not photobleach, and thereby enable longer measurement durations. Additionally, they offer reduced phototoxicity, allow short exposure times due to an increased photon budget, enable higher axial precision, and potentially simplify multiplexed imaging.
We adapted a 2D DNA origami structure with well-defined binding sites, spaced 40 and 60 nm apart, as a model system to demonstrate the feasibility of our approach. The GNPs were functionalized to transiently bind to these docking sites. We constructed a dual-modality iSCAT microscope capable of detecting 20 nm GNPs and performing simultaneous fluorescence measurements. Theoretical simulations of the point spread functions (PSFs) predicted a contrast of approximately 8% under ideal conditions, which we compared with our experimental results. To characterize the aggregation behavior of the functionalized GNPs, we performed dynamic light scattering (DLS) measurements under various salt concentrations, pH values, and functionalization protocols.
We demonstrated that our setup is capable of detecting 20 nm GNPs, although further improvements in axial focusing are necessary. DNA origami structures were successfully synthesized and detected using conventional DNA-PAINT. Gel electrophoresis confirmed that they remained stable even in low magnesium buffer conditions. We found that aggregation of GNPs occurs significantly faster in the presence of divalent cations compared to monovalent ions, with aggregation thresholds observed at 10 mM $MgCl_2$ and 500 μM $ZnCl_2$, while remaining stable up to 1 M NaCl and KCl. Lowering the pH was observed to further reduce aggregation.
These findings establish a robust experimental foundation for combining iSCAT with DNA-PAINT and lay the groundwork for future developments, including improved label specificity, advanced multiplexing strategies, and automated particle tracking algorithms.

Kurzfassung

Die Lichtmikroskopie gehört weiterhin zu den wichtigsten Werkzeugen zur Untersuchung der mikroskopischen Welt. Da die zu untersuchenden Proben immer kleiner, die ablaufenden Prozesse schneller und die experimentellen Umgebungen zunehmend komplexer werden, müssen sich mikroskopische Techniken entsprechend weiterentwickeln. In dieser Arbeit wird die Kombination der superauflösenden Technik DNA-PAINT mit der hochempfindlichen interferometrischen Streumikroskopie (iSCAT) untersucht. Als Marker wurden elastisch streuende Goldnanopartikel (GNPs) mit einem Durchmesser von 20 nm verwendet.
Wir gehen davon aus, dass diese Kombination mehrere Vorteile bietet: GNPs sind weniger anfällig für Umwelteinflüsse als viele fluoreszierende Marker, unterliegen keiner Photobleiche und ermöglichen dadurch längere Messzeiten. Zudem reduzieren sie die Phototoxizität, erlauben aufgrund eines erhöhten Photonbudgets kürzere Belichtungszeiten, bieten eine höhere axiale Auflösung und könnten die multiplexe Bildgebung vereinfachen.
Als Modellsystem zur Demonstration der Umsetzbarkeit unseres Ansatzes haben wir eine 2D-DNA-Origami-Struktur mit definierten Bindungsstellen im Abstand von 40 und 60 nm angepasst. Die GNPs wurden funktionalisiert, um transient an diese Dockingstellen zu binden. Es wurde ein dual-modales iSCAT-Mikroskop aufgebaut, das sowohl die Detektion von 20 nm großen GNPs als auch simultane Fluoreszenzmessungen ermöglicht. Theoretische Simulationen der Punktspreizfunktionen (PSFs) sagten einen Kontrast von etwa 8 % unter idealen Bedingungen voraus, der mit den experimentellen Ergebnissen verglichen wurde. Zur Charakterisierung des Aggregationsverhaltens der funktionalisierten GNPs wurden dynamische Lichtstreumessungen (DLS) unter verschiedenen Salzkonzentrationen, pH-Werten und Funktionalisierungsprotokollen durchgeführt.
Wir konnten zeigen, dass unser Aufbau in der Lage ist, 20 nm große GNPs zuverlässig zu detektieren, wenngleich eine Verbesserung der axialen Fokussierung notwendig ist. DNA-Origami-Strukturen wurden erfolgreich synthetisiert und mittels konventionellem DNA-PAINT nachgewiesen. Gelelektrophorese bestätigte ihre Stabilität auch bei Puffern mit geringer Magnesiumkonzentration. Es zeigte sich, dass GNPs in Anwesenheit zweiwertiger Kationen deutlich schneller aggregieren als bei einwertigen Ionen, wobei Aggregationsschwellen bei 10 mM $MgCl_2$ und 500 μM $ZnCl_2$ beobachtet wurden, während sie bis zu 1 M NaCl und KCl stabil blieben. Eine Absenkung des pH-Werts verringerte die Aggregation zusätzlich.
Diese Ergebnisse bilden eine solide experimentelle Grundlage für die Kombination von iSCAT und DNA-PAINT und schaffen die Basis für zukünftige Entwicklungen wie eine verbesserte Markerspezifität, erweiterte Multiplexing-Strategien und automatisierte Partikelverfolgungsalgorithmen.

List of Abbreviations

Microscopy Techniques and Terms

STED	Stimulated Emission Depletion Microscopy
PALM	Photo-Activated Localization Microscopy
dSTORM	Direct Stochastic Optical Reconstruction Microscopy
SIM	Structured Illumination Microscopy
DNA-PAINT	DNA Points Accumulation for Imaging in Nanoscale Topography
iSCAT	Interferometric Scattering Microscopy
PSF	Point Spread Function

Buffers and Chemical Compounds

PBS	Phosphate-Buffered Saline
NaCl	Sodium Chloride
KCl	Potassium Chloride
$MgCl_2$	Magnesium Chloride
$ZnCl_2$	Zinc Chloride
HCl	Hydrochloric Acid
NaOH	Sodium Hydroxide
EDTA	Ethylenediaminetetraacetic Acid

Data Analysis and Optics

DoG	Difference of Gaussian
CMOS	Complementary Metal-Oxide-Semiconductor
FPN	Fixed Pattern Noise
FFT	Fast Fourier Transformation
ACF	Autocorrelation Function
SNR	Signal-to-Noise Ratio
RDA	Rolling Differential Average
Speckle	Noise-like interference patterns from overlapping fields

Biology and DNA Terms

dsDNA	Double-Stranded DNA

ssDNA	Single-Stranded DNA
BSA	Bovine Serum Albumin

Physical and Statistical Terms

RMS	Root Mean Square
TEM00	Transverse Electromagnetic Mode 00

Other Terms

GNP	Gold Nanoparticle
ATTO655	A fluorescent dye used in DNA-PAINT

Chapter 1

Introduction

Light microscopy is one of the most important methods to analyze the microscopic world. As the samples we want to understand become smaller, we reach a point in which we are confronted with studying structures far smaller than the wavelength of the imaging radiation. This clashes with the classical Abbe resolution limit which is at approximately half the illumination wavelength. Super resolution microscopy pushes precisely this limit. Various techniques achieving super resolution microscopy have been developed, such as stimulated emission depletion (STED)[18], photo-activated localization microscopy (PALM)[3], [19], direct stochastic optical reconstruction microscopy (dSTORM)[17], [55], and structured illumination microscopy (SIM)[16], to name a few.
This thesis will focus on a super resolution technique called DNA points accumulation for imaging in nanoscale topography (DNA-PAINT) [31], [39] and the highly sensitive interferometric scattering (iSCAT) microscopy[34], [50]. The goal is to utilize both Rayleigh scattering from iSCAT as well as the stochastic super resolution technique called 'blinking' from DNA-PAINT to push the boundaries of spatial and temporal resolution. Using gold nanoparticles (GNPs) as labels can simplify measurements, as gold scatters at any wavelength and gold scattering properties are less affected by environmental factors such as pH, oxygen levels, heat, enzymes, gases, or ion concentrations compared to fluorescent labels[8]. Additionally, gold does not bleach. Implementing iSCAT in DNA-PAINT also offers the advantage of high axial precision, reaching several nanometers [46], [54]. Moreover, the ability to use short exposure times - around 5 ms in our case, though it can be reduced by an order of magnitude and more depending on the laser power - could be beneficial for capturing nanometer-scale movements during imaging. The proof of principle we aim to demonstrate is the detection of a 2D rectangular DNA origami structure measuring 40 $\times$ 60 nm.

Main results

This work established the feasibility of combining iSCAT with DNA-PAINT by systematically addressing the key requirements for future proof-of-principle experiments. We developed a dual-modality microscope capable of both iSCAT and fluorescence imaging, successfully demonstrating detection of 20 nm ssDNA-functionalized GNPs. The experimental framework was built around 40 $\times$ 60 nm rectangular DNA origami structures featuring four precisely positioned docking sites, whose proper folding and spatial organization were verified through DNA-PAINT control experiments using fluorescent labels. *Nanobem* simulations provided theoretical validation, predicting an 8% contrast for 20 nm

GNPs under ideal imaging conditions. Comprehensive characterization of GNP behavior revealed that ssDNA functionalization significantly improved GNP stability, with DLS measurements showing resistance to aggregation up to 1 M NaCl/KCl, while identifying aggregation thresholds at 10 mM $MgCl_2$ and 500 μM $ZnCl_2$. Notably, unfunctionalized citrate-stabilized GNPs showed much lower stability, aggregating at just 2.5 mM $MgCl_2$. We further discovered that lower pH conditions could mitigate Mg^{2+}-induced aggregation. To address the challenges of nanoparticle detection, we implemented and optimized noise-reduction algorithms including differential averaging and Fourier filtering. Together, these results establish a robust experimental and analytical foundation for future iSCAT-based DNA-PAINT implementations, while highlighting specific pathways for improvement through functionalization optimization, nonspecific binding reduction, and advanced particle tracking methodologies.

Thesis structure

In chapter 2, a brief summary of the theoretical concepts that are necessary to understand for this thesis will be introduced, including DNA-PAINT, iSCAT, DNA Origami, and DLS. Chapter 3 will explain the experimental setup, detailing the combination of iSCAT with DNA PAINT, the design of DNA Origami, the use of gold GNPs, data analysis methods, and DLS measurements of the GNPs. Chapter 4 will present the results, including the detection of GNPs, DNA Origami production, DLS measurements, and the challenges encountered during iSCAT measurements. It will discuss the implications of the results, particularly focusing on the behavior of DNA Origami and GNPs under different conditions. Finally, Chapter 5 will summarize the findings and provide an outlook on potential future improvements in the experimental setup and methodologies.

Chapter 2

Theory

In this project, we combine the super-resolution techniques iSCAT and DNA-PAINT, to achieve our research objectives. To provide the necessary context, we will briefly introduce the principles of both methods. Since DNA origami structures play a crucial role in our measurement setup, a concise overview of their concept will also be provided. Additionally, Dynamic Light Scattering (DLS) was employed as an essential tool for analyzing the characteristics of gold GNPs; therefore, the underlying concept of DLS will be introduced as well.

2.1 DNA-PAINT

In 1962 scientist Osamu Shimomura first described a green fluorescent protein he found in jellyfish[43]. Approximately thirty years later, this fluorescent protein was used as a tag to localize and track proteins within cells[6]. Since then, research in the field of fluorescent microscopy has exploded. A big challenge was to overcome the Abbe resolution limit, which makes it impossible to decipher between two tags below a distance of approximately half the imaging wavelength. In 2006 Eric Betzig managed to push beyond the resolution limit by relying on a method that turns the fluorescence of individual molecules on and off. This is called 'blinking'. For this achievement, Betzig, along with William Moerner and Stefan Hell, received the Nobel prize in Chemistry in 2014. Blinking allows the sub wavelength resolution, by not activating all dyes at the same time. This makes it possible to distinguish two dyes with distance smaller than the diffraction limit. This blinking can be achieved in various ways, briefly described below.
One method involves randomly keeping the fluorescent molecules predominantly in a non-emissive state, ensuring that within a 200 nm radius, statistically only one emitter is active at any given time. This is what is done in photoactivated localization microscopy (PALM) employing fluorescent proteins[3] and stochastic optical reconstruction microscopy (STORM) employing organic dyes[17], [55].
Unlike techniques that rely on permanently bound fluorophores that stochastically photoactivate, PAINT utilizes freely diffusing dyes that transiently bind to the target molecules. The key idea is to use fast and transient binding events, where the dyes diffuse freely in the buffer solution and only emit detectable signals when bound to the target. In the unbound state, the dyes move rapidly and diffuse over numerous camera pixels during the duration of a single frame, making their signal undetectable. However, when a dye transiently binds to the target molecule, it becomes immobilized, allowing the camera to accumulate enough photons to localize the dye with high precision. Through this mecha-

nism, the object of interest is continuously probed by the dyes, enabling super-resolution imaging.
The flux of incident dyes depends on the concentration of the dyes in solution and their diffusion coefficient. For example, the original PAINT method introduced by Sharonov and Hochstrasser relied on hydrophobic interactions between the dye and the target molecules, such as lipid membranes[42]. While this approach works well for hydrophobic targets, it lacks specificity for more complex biological structures. To address this limitation, DNA-PAINT was developed, which uses DNA hybridization as the binding mechanism. As described by Schnitzelbauer et al. [39], in DNA-PAINT, short DNA strands (docking strands) are attached to the target molecules, and complementary DNA strands (imager strands) labeled with fluorophores transiently bind to these docking sites. This approach provides precise control over binding events, as the binding affinity and duration can be tuned by adjusting the DNA sequence length, salt concentration, and temperature.

2.2 iSCAT

One of the biggest limitations of fluorescent labels is their susceptibility to photobleaching, which restricts the observation time. In contrast, a scattering signal does not bleach, because the illumination light typically scatters elastically with the sample, enabling prolonged measurement periods [50]. In dark-field microscopy, the signal ideally consists solely of the scattered field. Using this technique, gold nanoparticles with diameters as small as 40 nm have been measured [1], [21], [33]. However, detecting smaller particles is challenging because the intensity of the scattered signal $I = |\bar{E}_s|^2$ diminishes proportional to the sixth power of the radius of the particles. For instance, reducing the size from 60 nm to 6 nm decreases the signal intensity by a factor of one million.

In contrast, iSCAT can measure nanoparticles as small as 6 nm, with gold nanoparticles as small as 2 nm in diameter having been detected [7], [21]. This capability is achieved by introducing a reference field. The following section delves into the principles of iSCAT.

2.2.1 Foundations

The basic iSCAT setup is illustrated in Figure 2.1. Using the scalar wave model of light, we can describe the propagation of light as $\bar{E}(\vec{r}, t) = E_0\, e^{i(\vec{k}\cdot\vec{r}-\omega t+\phi)}$, where $\bar{E}(\vec{r}, t)$ denotes the scalar electric field at position $\vec{r}$ and time t, E_0 denotes the amplitude of the wave, $\vec{k}$ denotes the wave vector, ω denotes the angular frequency, and ϕ denotes the phase. In iSCAT, the detected intensity I_d comprises contributions from both the scattered signal $\bar{E}_s$ and the reflected signal $\bar{E}_r$. This relationship is illustrated in Figure 2.2 and is expressed by the formula:

$$I_d \propto |\bar{E}_s + \bar{E}_r|^2 = |E_s|^2 + |E_r|^2 + 2E_sE_r\cos(\phi), \tag{2.1}$$

where $\phi = \phi_r - \phi_s$. This phase ϕ includes several components:

1. **Geometrical phase shift**: Arising from the optical path length difference between the two beams, this contribution depends on the axial position of the scatterer, the refractive index n of the medium and the wavelength of the illumination light. Furthermore, when a beam passes through a focus, it experiences a so-called Gouy phase shift of π [15].

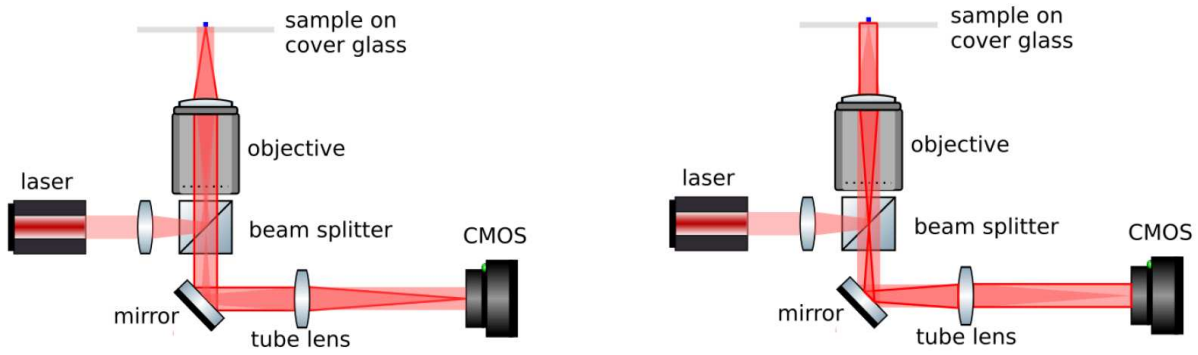

(a) Scattered field (b) Reference field

Figure 2.1: **Principle Setup of Bright-Field iSCAT** [35]. Coherent laser light is focused on the back focal plane of an objective. A portion of this light is reflected by a cover glass, forming the reference field, while another portion scatters at the sample on the cover glass, generating the scattered field. The scattered field is directed and focused onto the detector, a CMOS camera in this case, using a beam splitter, mirror, and tube lens. At the detector, the scattered field interferes with the reference field.

2. **Phase shift due to polarizability**: The polarizability α of the particle is generally complex and introduces a phase shift into the scattered field relative to the incident field. Since the scattered field is proportional to the induced dipole, $E_s \propto \alpha E_i$, its phase becomes shifted by $\arg(\alpha)$ with respect to the incident field. This phase shift directly enters the interference term and can significantly affect the iSCAT signal.

   The polarizability is given by

$$\alpha = 3\epsilon_m V \left(\frac{\epsilon_p - \epsilon_m}{\epsilon_p + 2\epsilon_m} \right), \tag{2.2}$$

   where V is the particle volume, and $\epsilon_p = \epsilon_p' - i\epsilon_p''$ and ϵ_m are the complex, wavelength-dependent permittivities of the particle and the surrounding medium, respectively. For spherical gold nanoparticles with a radius of 10 nm in phosphate-buffered saline (PBS), and at an illumination wavelength of 465 nm, we estimate the dielectric function of gold as $\epsilon_p \approx -1.54 + 2.41i$ [22], and $\epsilon_m \approx 1.77$. This yields a complex polarizability with a phase shift of approximately

$$\arg(\alpha) \approx 0.52\,\pi. \tag{2.3}$$

   This fixed offset is a significant contribution to the total phase ϕ and must be taken into account when interpreting the iSCAT interference pattern.

These components together determine the total phase ϕ, which plays a crucial role in the interference pattern observed in iSCAT.
The critical variable responsible for generating the signal on the detector is the scattered field $E_s = \alpha E_i$, as discussed above. The magnitude of the polarizability governs the strength of the scattered field and, thereby, the amplitude of the interference term. While high reflectivity and low absorption (as in gold or silver) improve signal strength, the dominant factor determining scattering efficiency at this scale is particle volume [50]. The enhanced intensity observed in iSCAT for small particles, compared to dark-field

microscopy, can be attributed to the interference-induced cross term $2E_sE_r\cos(\phi)$. This term explains why the signal is proportional to the third power of the radius of the particle, rather than the sixth power as dictated by $I_s = |\bar{E}_s|^2$. Consequently, as we aim to measure increasingly smaller particles, the cross-term in equation 2.1 starts dominating, such that $I_d - I_r \approx 2E_sE_r\cos(\phi)$. The contrast c of the PSF of a nanoparticle, when compared to an image without a nanoparticle reads

$$c = \frac{2E_sE_r\cos(\phi)}{I_r} = 2\frac{E_s}{E_r}\cos(\phi). \tag{2.4}$$

A superficial evaluation of this equation might misleadingly suggest that minimizing the reference field E_r would enhance sensitivity. However, decreasing $|E_r|$ comes at the cost of reducing the overall signal leading to a smaller signal to noise ratio (SNR) in shot-noise-limited detection [49].
There are different setups to superimpose the scattering field with the reference field, as shown in Figure 2.2. The back reflection scheme shown in Figure 2.2b introduces a sensitivity in the z-direction, i.e. perpendicular to the coverslip, of several nanometers [46], [54]. This is useful if high axial precision is needed.

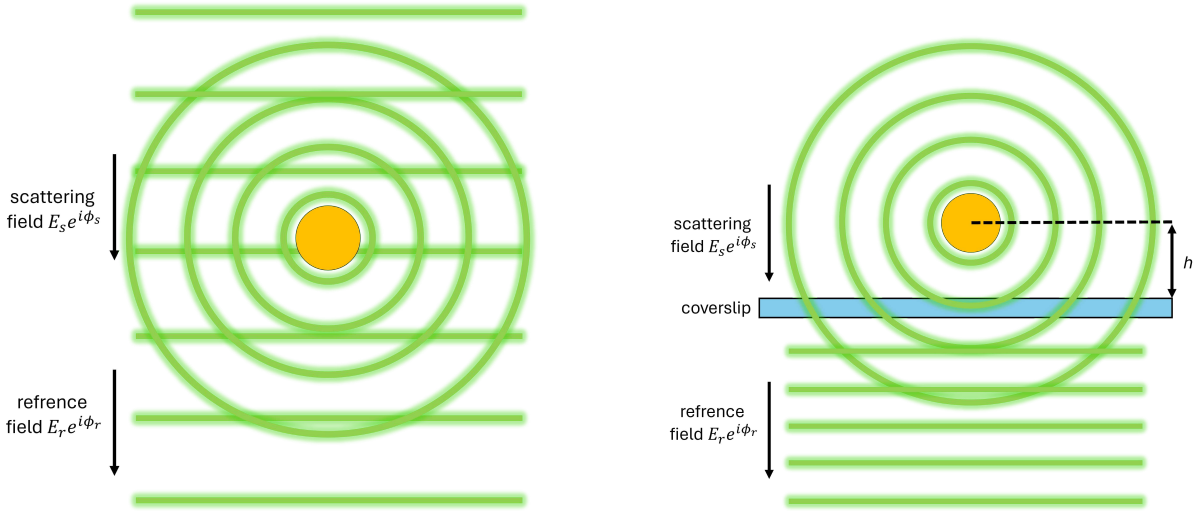

(a) (b)

Figure 2.2: **Two different realizations of interferometric scattering.** The green lines and circles represent the electromagnetic field lines. The yellow circle the scattering object. (a) depicts conventional bright-field imaging. The scattering field $E_se^{i\phi_s}$ is superimposed on the reference field $E_re^{i\phi_r}$. (b) depicts a back reflection scheme, enabling high axial resolution.

2.2.2 Noise

As we strive for higher detection sensitivity in iSCAT measurements, we encounter both technical challenges and fundamental limits. The primary limiting factor is signal fluctuation. While slow signal fluctuations, such as drift or gradual changes in laser intensity, can be corrected either post-process or during measurement, the fast and random fluctuations, known as noise, primarily determine the detection sensitivity and the spatial and temporal resolution. This section provides an overview of the types of noise encountered

in iSCAT measurements.

One significant issue is **laser intensity fluctuations** caused by inevitable imperfections in laser design. Instrumental laser intensity fluctuations can be minimized to 10^{-7} RMS [38]. However, available light sources often exhibit intensity fluctuations greater than 0.1% [12]. These fluctuations can be managed using a proportional-integral-derivative control loop, stabilizing the intensity to the order of 10^{-4} [34]. Depending on the required sensitivity, power-normalization can be applied post-measurement during data processing.

Even if instrumental signal fluctuations are addressed, the intrinsic limit of **shot noise** remains a challenge for all coherent light sources, following the Poisson distribution:

$$P(n) = |\langle n|\alpha\rangle|^2 = e^{-\langle n\rangle}\frac{\langle n\rangle^n}{n!}, \tag{2.5}$$

where $P(n)$ is the probability distribution of detecting n photons in a given time interval, $|n\rangle$ is a quantum state vector in the Fock basis, representing a state with exactly n photons, $\langle n\rangle$ is the expectation value of the number of photons in a given state, representing the average number of photons we would expect to detect over many measurements, and $|\alpha\rangle = e^{-\frac{|\alpha|^2}{2}}\sum_{n=0}^{\infty}\frac{\alpha^n}{\sqrt{n!}}|n\rangle$ defines a coherent state. For a large number of photons, we can approximate the signal-to-noise ratio of the detected photon count to $SNR = \frac{N}{\sqrt{N}} = \sqrt{N}$, where N is the average number of detected photons. Shot noise can be reduced by increasing the number of frames over which averaging is performed, although this comes at the expense of lower temporal resolution.

Another limiting factor is **digitalization noise** imposed by the measuring device, such as dark noise or reading errors. Additionally, the bit depth of the camera, which discretizes the gray levels, and the pixel discretization in the x and y directions, also contribute to detection limits. These limitations can be significantly mitigated by applying a fit to the point spread function (PSF), as discussed in detail in Section 3.3.1.

The largest signal fluctuations arise from the **material features of the setup**, such as the roughness of the coverslip, dust in the optical setup, or in the buffer solution. These factors generate a speckle-like background, making it challenging to distinguish a speckle from a static particle if the particle has too low a contrast.

2.3 DNA Origami Principle

The performance of our microscope and data analysis tools can be confirmed only when we are confident in the integrity of the measured sample. Therefore, we require highly reliable nanostructures as positive controls. DNA Origami is a method invented by Rothemund in 2006 [37] that is not only reliable, but also established, quick, straight-forward, and cheap. It can produce almost arbitrarily complex nanostructures. The idea is to take advantage of the self-assembly of DNA molecules: A multiple kilo-bases long, single strand DNA (ssDNA) molecule called a scaffold is mixed with hundreds of short oligonucleotide 'staple strands' in a folding buffer solution (12.5 mM $MgCl_2$, 10 mM Tris and 10 mM EDTA at pH 8.0) and then exposed to a high temperature of 80 °C, a temperature at which DNA can not form double strands (dsDNA), ensuring the DNA remains single stranded. Then, the temperature is set to 60 °C and in steps of 1 °C slowly cooled to 4 °C. For more details,

see 6.3. During this controlled temperature ramp, the staple strands hybridize to the scaffold, pinching it into a desired shape. Not only is it possible to create nanostructures, but one can functionalize them using so called 'handles' and 'anti-handles': One part of a ssDNA hybridizes with the surface of the DNA Origami. The other part of this handle is then used as a docking station for an anti-handle with a complementary sequence. To this anti-handle, one can now attach a guest molecule via covalent linkage, like a protein, a fluorescent die, or a gold nanoparticle (GNP). The length of the sequence of the anti-handle, its CG content and the surrounding pH level and salt concentrations determine the length of the transient interaction that can range from nanoseconds to permanent binding. Find more specific and quantitative information on binding length in [41], [47].

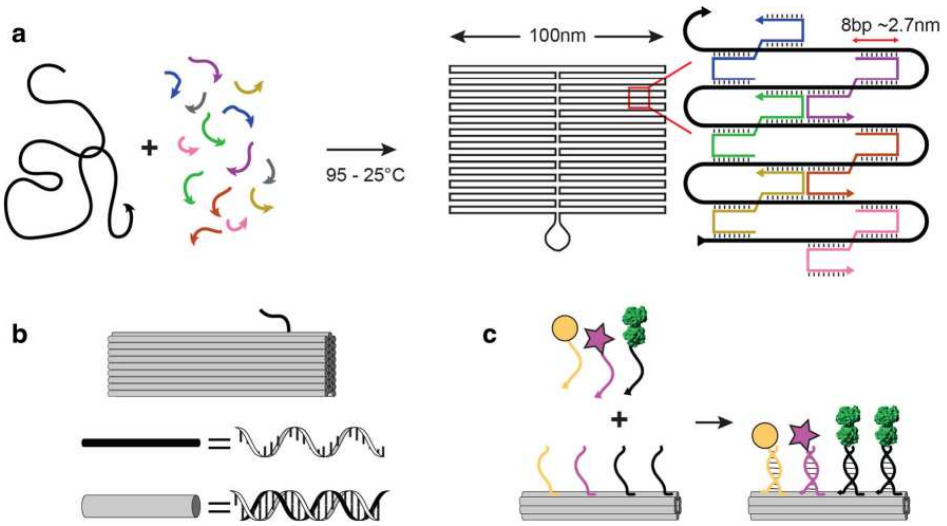

Figure 2.3: Depiction of DNA Origami nanostructures (adapted from from Singh et. al 2018 [44]). (a) Shows the scaffold (black) and the staple strands (various colors) as single strands before hybridization (top left) and in hybridized state (top right). (b) Double strands are represented as rigid cylinders that have a diameter of 2.6 nm, while the flexible ssDNAs are represented by thinner black lines. (c) Demonstrates handles attached to the DNA Origami and anti-handles bound to guest molecules (gold nanoparticles, fluorescent dies, proteins, etc.) in an unbound state (left) and a bound state (right).

2.4 DLS

2.4.1 Introduction

DLS is a powerful technique to measure size distributions of small particles in suspension. In our case, determining the size distribution of uniformly sized GNPs provides insight into the extent of aggregation under different buffer conditions. DLS measures the translational diffusion of particles due to Brownian motion. Exposing the particles to light will generate fluctuations in intensity of the scattered light, which can be analyzed with the help of the autocorrelation function and the Stokes-Einstein relationship, which will be discussed in further depth in the following sections.

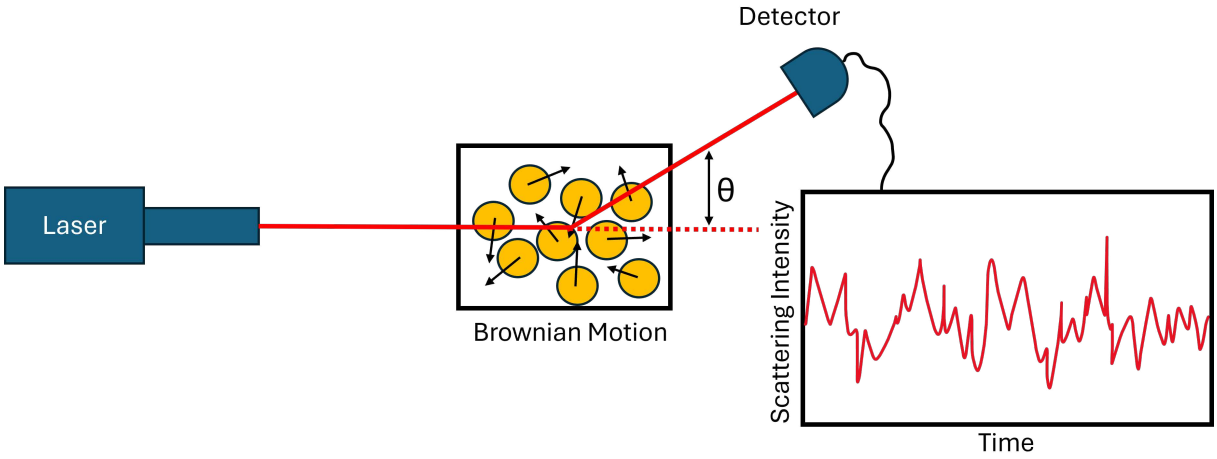

Figure 2.4: **Principle of dynamic light scattering:** Laser light scatters from the sample in solution, creating a noise-like intensity signal.

2.4.2 Dynamic light scattering (DLS) principle

The principle of DLS can be seen in Figure 2.4. A laser illuminates a volume carrying the sample in solution. A detector sits at an angle θ to measure the time-dependent intensity $I(\theta, t)$ of the scattered light. As the particles of interest undergo Brownian motion, the intensity of the scattered light fluctuates with time. The signal is analyzed with the autocorrelation function, while the hydrodynamic radius is calculated using the Stokes-Einstein equation.

2.4.3 Autocorrelation Function

This section follows Chapter 2 of [2]. In dynamic light scattering (DLS), the intensity fluctuations $I(t)$ appear random and noise-like, but they contain information about the motion of the particles. To analyze these fluctuations, we use the autocorrelation function (ACF), which quantifies how the intensity at a given time t is correlated with the intensity at a later time $t + \tau$. The ACF is defined as:

$$f(\tau) = \langle I(t)I(t+\tau)\rangle,$$

where $\langle\cdot\rangle$ denotes the time average, and τ is the time delay. For small time delays τ, the intensity $I(t + \tau)$ is likely to be similar to $I(t)$, meaning the correlation is high. As τ increases, the correlation decreases because the particles move and the intensity fluctuations become less related. The ACF therefore decays over time, and the rate of decay depends on the size of the particles: smaller particles diffuse faster, causing the ACF to decay more quickly, while larger particles diffuse more slowly, resulting in a slower decay.

The ACF for particles undergoing Brownian motion follows an exponential decay:

$$f(\tau) = \langle I\rangle^2 + (\langle I^2\rangle - \langle I\rangle^2)\exp\left(-\frac{\tau}{\tau_r}\right),$$

where τ_r is the relaxation time, which is related to the diffusion coefficient of the particles.

- At $\tau = 0$, the signal is perfectly correlated, meaning $I(t + \tau) = I(t)$. This corresponds to the maximum value of the ACF:

$$f(0) = \langle I^2 \rangle.$$

  Here, $\langle I^2 \rangle$ represents the mean squared intensity, which reflects the total power of the signal.

- As τ increases, the correlation between $I(t)$ and $I(t+\tau)$ decreases. At $\tau \to \infty$, the signal becomes completely uncorrelated, and the ACF reaches its baseline value:

$$f(\tau \to \infty) = \langle I \rangle^2.$$

  Here, $\langle I \rangle^2$ represents the square of the mean intensity, which is the baseline value of the ACF when no correlation remains.

An example of an ACF with its limits is shown in Figure 2.5.

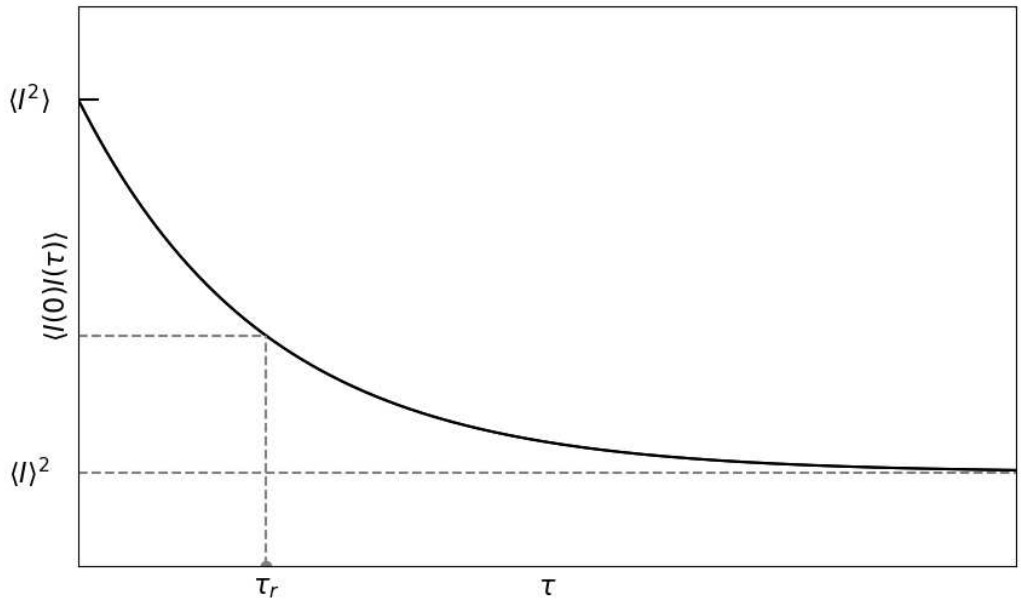

Figure 2.5: Visualization of the autocorrelation function $\langle I(0)I(\tau) \rangle$.

To facilitate the comparison of different ACFs, it is standard practice to normalize them. This is done by dividing the ACF by its value at $\tau = 0$. The normalized autocorrelation function $g(\tau)$ is then given by:

$$g(\tau) = \frac{f(\tau)}{f(0)} = \frac{\langle I \rangle^2 + (\langle I^2 \rangle - \langle I \rangle^2) \exp\left(-\frac{\tau}{\tau_r}\right)}{\langle I^2 \rangle}.$$

This can be rewritten as:

$$g(\tau) = \frac{\langle I \rangle^2}{\langle I^2 \rangle} + \left(1 - \frac{\langle I \rangle^2}{\langle I^2 \rangle}\right) \exp\left(-\frac{\tau}{\tau_r}\right).$$

The normalized autocorrelation function starts at 1 when $\tau = 0$ and decays to $\frac{\langle I \rangle^2}{\langle I^2 \rangle}$ as $\tau \to \infty$. The decay is governed by the exponential term: the ACF of small particles decays quickly, while the ACF of large particles decays slowly. An example is sketched in Figure 2.6. This allows for the analysis of particle size, as will be discussed in the next chapter.

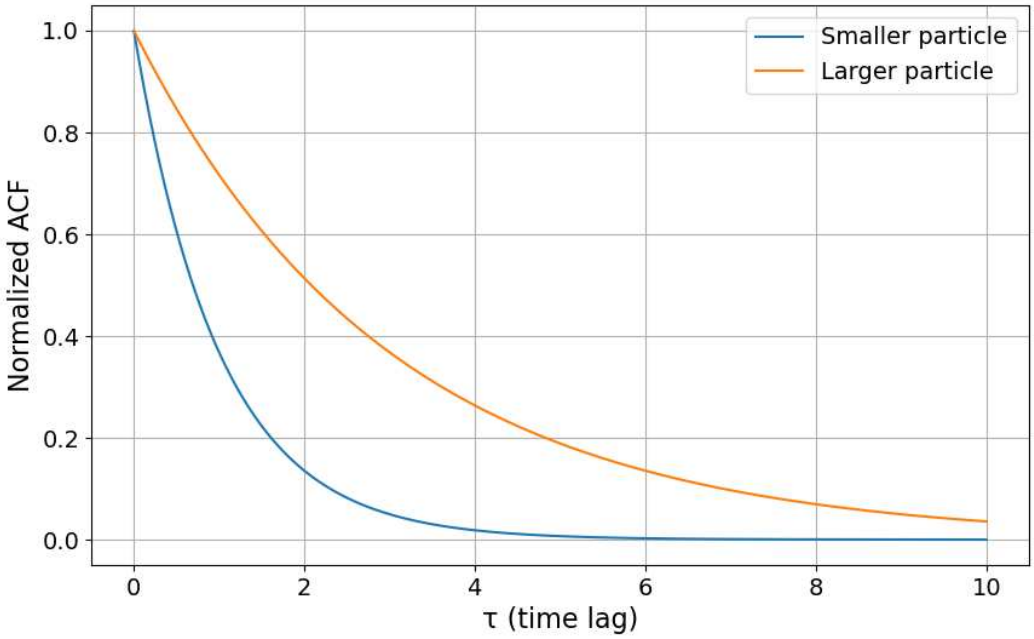

Figure 2.6: ACFs with different relaxation times. The blue curve represents a smaller particle, as the correlation drops more quickly compared to the orange curve, which represents a larger particle.

2.4.4 Stokes-Einstein Relationship

Recalling equation 2.4.3, the normalized ACF can be written in the form

$$f(\tau) = \beta + (1 - \beta) \exp\left(-\frac{\tau}{,}\tau_r\right). \tag{2.6}$$

where β depends on the experimental starting conditions. The exponential $\exp\left\{-\frac{\tau}{\tau_r}\right\}$ is also called the dynamic structure factor, where

$$\tau_r^{-1} = |\vec{q}|^2 D_0. \tag{2.7}$$

Here, D_0 denotes the translational diffusion coefficient. $\vec{q}$ is called the scattering vector, defined in terms of the scattering geometry as the difference of the incident wave vector and the scattering wave vector $\vec{q} = \vec{k}_i - \vec{k}_s$. The absolute value of the scattering value is

$$|\vec{q}| = \frac{4\pi n}{\lambda} \sin\frac{\theta}{2}. \tag{2.8}$$

Here, λ is the wavelength of the incident light, ϕ is the angle between $\vec{k}_i$ and $\vec{k}_s$, which is determined by the position of the detector relative to the incident beam, and n is the refractive index of the scattering medium. The Einstein equations relate the diffusion coefficient to

$$D_0 = \frac{k_B T}{\zeta}, \tag{2.9}$$

where k_B is the Boltzmann constant, T is the temperature, and ζ is the friction constant. Using the Stokes approximation, we he have $\zeta = 6\pi\eta R_H$, where η is the viscosity, and R_H the hydrodynamic radius. Finally, by combining the Einstein equations and the Stokes approximation, we have the Stokes-Einstein equations:

$$R_H = \frac{k_B T}{6\pi\eta D_0}. \tag{2.10}$$

In summary, after conducting a DLS measurement, we can calculate the ACF. Then we can fit the ACF with equation 2.6, and calculate the hydrodynamic radius using the Stokes-Einstein equations.

Chapter 3

Methods

3.1 Setup

A top view of our setup, is shown in Figure 3.1. The principle design is shown in Figure 3.2. The setup has three main channels: an iSCAT channel, a fluorescent channel, and an autofocus channel.

The **iSCAT channel** utilizes a Sparrow OEM laser module equipped with a Nichia NUBM07E laser diode. The laser emits at a wavelength of 450 nm with a maximum output power of 4.5 W in continuous wave (CW) mode. The laser beam has a Gaussian profile with a divergence of approximately 1.5 mrad. The beam is directed through two mirrors into a polarization-maintaining optical fiber, which serves as a spatial filter. The fiber's damage threshold limits the input power to approximately 300 mW. Combined with the low transmission efficiency of the fiber, this limits the output intensity to around 80 mW. The iSCAT and fluorescence paths are combined using mirrors and a dichroic mirror. The light then passes through a Zeiss tube lens with a focal length of 164.5 mm, which is positioned to focus on the back focal plane of a 60x apochromat objective with a numerical aperture of 1.42. The sample stage, holding a glass coverslip of 170 $\pm$ 5 μm thickness, allows movement in both planar and axial directions. The illumination path is separated from the detection path by a non-polarizing plate beam splitter with a 90/10 splitting ratio, while a second dichroic mirror further separates the iSCAT path from the fluorescence path. The detection light passes through a second tube lens to focus the image onto a photonfocus CMOS camera, with a 4f system introducing a magnification of $M = \frac{f_2}{f_1} = \frac{200\,\text{mm}}{75\,\text{mm}} = \frac{8}{3}$. The 4f system consists of two achromatic doublet lenses with focal length of 75 mm and 200 mm. Achromatic doublet lenses are less sensitive to misalignment along the beam axis. This is important in iSCAT, as the beam is typically slightly misaligned to prevent interference from reflections within the objective lens, meaning the setup must accommodate off-axis beams.

The **fluorescent channel** employs a 642 nm Vortran Stradus TEM00 laser as its light source. The beam is directed into a single-mode fiber acting as a spatial filter. At the end of the fiber is a 4x objective with an optical aperture of 0.1 positioned to focus the beam on the back focal plane of the imaging objective. Since the fluorescence path passes through the same tube lens as the iSCAT path, a 15 mm focal length lens is used to counteract the effect of the tube lens. A third dichroic mirror is used to separate the fluorescent signal from the iSCAT signal and direct them to the detector. Another beam splitter directs part of the fluorescent signal to the autofocus detector. The autofocus channel is designed to maintain focus by analyzing the position of light reflected at an

oblique angle. While the autofocus channel is integrated into the setup, it was not utilized for the experiments described in this thesis. Instead, focus adjustments were performed manually using the z-stage.

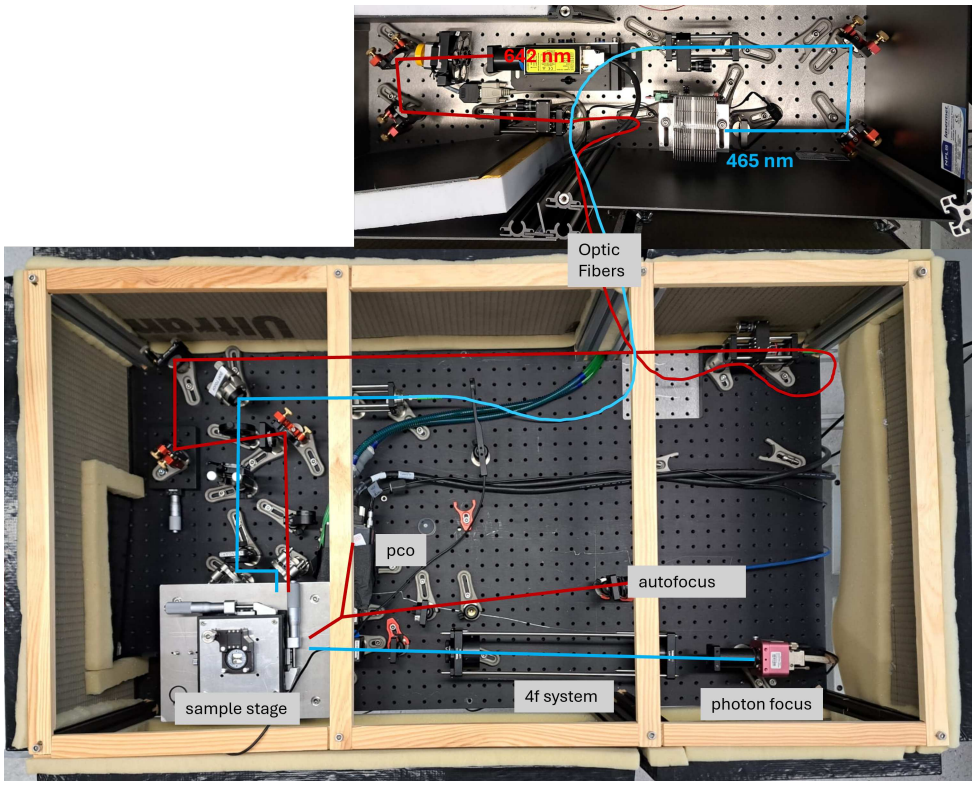

Figure 3.1: **Top view of iSCAT setup.** The paths of the red and blue lasers are highlighted.

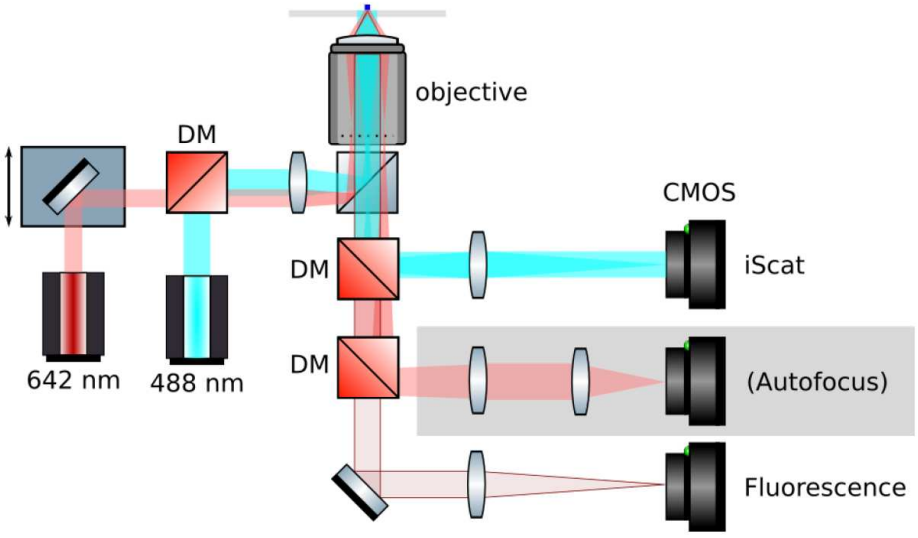

Figure 3.2: **Principle design of the iSCAT setup Platzer2024**.

3.2 Principle of combining iSCAT with DNA-PAINT

3.2.1 The DNA Origami Design

For our purposes, the DNA Origami serves as the positive control. Therefore, we want the sample design to be as straightforward as possible. We decided to follow a design from the Jungmann group [39]. They found a flat, rectangular 2D DNA origami structure with the dimensions 90x70 nm to be an ideal structure for DNA-PAINT imaging. The origami forms a 3x4 grid with 20 nm spacing between the grid points which are addressable by docking staple strands. The structure is shown in Figure 3.3. For the precise protocol, see appendix 6.3.

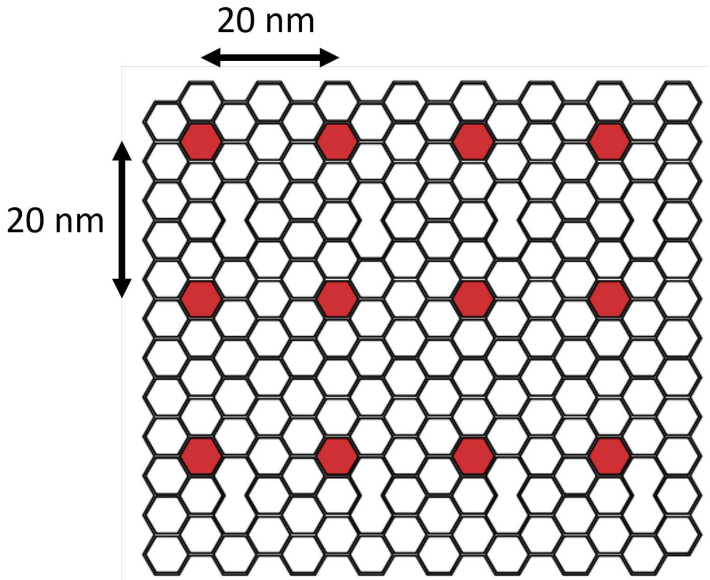

Figure 3.3: The DNA Origami showcased as a grid structure with 20 nm spacing between the grid points. This is taken from [39].

We incorporate three distinct functionalities into the DNA structure: anchoring handles designed as docking sites for gold labels, fluorescent dyes serving as validation controls, and biotin. The four corner points of the grid seen in Figure 3.3 serve as the designated docking sites for Gold labels, a concept elaborated upon in Section 3.2.2. This spatial arrangement defines a 40x60 nm rectangular region. We first attached fluorescent dyes to the gold docking sites to check if the DNA origamis assembled correctly, i.e. the desired geometry was achieved. The result can be seen in 4.2.1. The next step will be to detect this 40x60 nm rectangle using gold labels instead of fluorescent labels. The docking strands will be ssDNA handles of the sequence CTTCTTC, with the 5' end pointing towards the DNA Origami and the 3' end pointing away from the DNA Origami. The anti-handle to which the gold label will be attached will be the complementary sequence 5'-GAAGAAG-3'. The choice of sequence will be discussed in 3.2.2.
The iSCAT setup (see 3.1) enables simultaneous fluorescence microscopy and iSCAT measurements. This allows us to implement another method of validation to ensure that we are measuring our sample: To one of the two center points of the Origami grid we attach one Alexa Fluor 647 fluorescent label.
Finally, we need the DNA Origami to stick to the glass to prevent serious drift and ensure the right orientation: the docking sites should face away from the cover-slip. We coat the glass slide with BSA/biotin/streptavidin. Additionally, we attach eight biotinylated staple strands to the DNA Origami that can attach to the streptavidin from the glass coating. This ensures that the DNA Origami is immobile. See a sketch of the design in Figure 3.4.

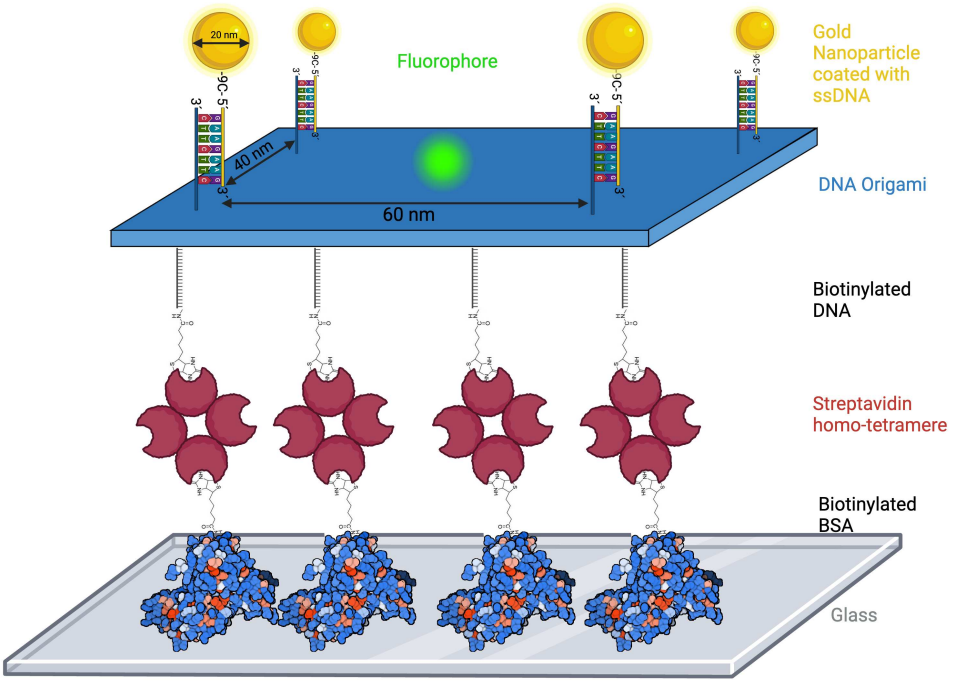

Figure 3.4: This image was created with BioRender.com. To ensure better visibility, the different molecules are not shown to scale.

3.2.2 Gold labels

For the elastically scattering labels, we chose GNPs of 20 nm diameter suspended in PBS that were functionalized with a seven base long ssDNA with the sequence GAAGAAG with a nine-cytosine (9C) linker. The ssDNA was attached to the GNPs via a thiol modification at the 5' end, which forms a stable bond with the gold surface. This sequence was chosen based on measurements by [47], which reported an event length of approximately 400 ms, corresponding to a K_{on} rate of 2.6 s^{-1} in an imaging buffer containing 1x PBS of pH 7.4 along with 500 mM NaCl. In our experiments, we expect a shorter event length since we will not add 500 mM NaCl to the PB: The reduction in salt concentration decreases the ionic strength of the buffer, which weakens electrostatic screening between the negatively charged DNA strands. This reduces the stability of the DNA interactions, leading to faster dissociation and shorter event lengths. Additionally, the event length will be influenced by the kinetics of the GNPs. However, we do not anticipate it to decrease by two orders of magnitude, which would be below our typical exposure time of 5 ms. Future measurements of the functionalized GNP event length will be necessary to confirm this assumption.

3.2.3 iSCAT DNA-PAINT principle

This section we propose the principle method on how to combine iSCAT with DNA-PAINT, shown in Figure 3.5. Similar to conventional DNA-PAINT, the GNPs will bind to one of the docking strands on one of the four corners of the DNA origami, as they are functionalized with the complementary DNA sequence. These binding events are transient, with GNPs detaching after a characteristic duration.
To analyze the data, we will use a differential rolling average, as implemented in the open source package PiSCAT [12]. This method calculates two rolling averages RA_t over a sliding window of frames:

$$\text{batch}_1 = \frac{1}{N} \sum_{i=t-N}^{t} I_i(x, y), \tag{3.1}$$

$$\text{batch}_2 = \frac{1}{N} \sum_{i=t+1}^{t+N+1} I_i(x, y), \tag{3.2}$$

where $I_i(x, y)$ is the intensity of the pixel at position (x, y) in frame i, N is the window size (batch size), and t is the current frame index. The differential image is then computed as:

$$\Delta I_t(x, y) = \text{batch}_2 - \text{batch}_1. \tag{3.3}$$

This subtraction removes static or slowly varying background signals, leaving only dynamic changes such as binding and unbinding events.
Depending on the axial focus, a binding GNP will exhibit a PSF with a bright center, while an unbinding GNP will display a PSF with a dark center, or vice versa. Specifically, when a GNP docks onto a docking site of the DNA origami, it is detected as a PSF with a bright center under the appropriate focus. The GNP remains bound for a characteristic lifetime before detaching, at which point it leaves a PSF with a dark center. This distinct behavior enables the differentiation of specific GNP-origami binding events from nonspecific interactions, such as GNPs adhering to the coverslip. The strong axial selectivity

inherent to iSCAT further restricts the detection of freely diffusing GNPs, enhancing the sensitivity to binding events. The concept is illustrated in Figure 3.5. A future task will involve developing an algorithm to reliably distinguish specific binding events from random or nonspecific interactions.

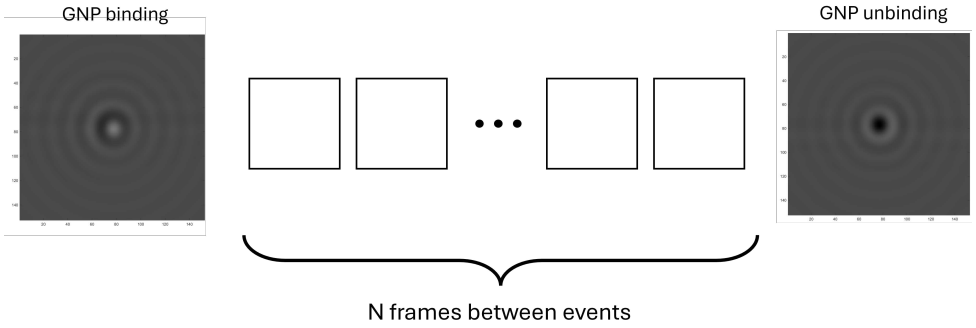

Figure 3.5: **Concept of iSCAT PAINT.** The simulated PSF of a 20 nm GNP binding on the left, and unbinding on the right. Between these two events a certain amount of frames have passed.

3.2.4 Sample preparation

We use Zeiss high performance 18 mm x 18 mm coverslip with a thickness of 0.17 mm. A procedure on how the coverslip is prepared before adding the GNPs is provided below:

Step 1: Clean the coverslip

We place the coverslip on a lens cleaning tissue. We fold another lens cleaning tissue twice and wet it with a couple of drops of methanol. We then carefully stroke the wet tissue over the coverslip on both sides. We hold the coverslip against the light to check for dust. We repeat the process until no dust can be detected visually.

Step 2: Attach silicone well

A silicone isolator with a pressure-sensitive adhesive (PSA) on one side and a diameter of 2,mm is placed in the center of the coverslip and gently pressed to secure it. PSA is a type of adhesive that bonds to surfaces upon application of light pressure, eliminating the need for solvents or heat. The silicone well has a capacity of 12 μl and provides a confined area for sample deposition.

Step 3: Place coverslip into stage

Step 4: BSA-Biotin-Streptavidin Layer Preparation

To immobilize the DNA Origamis and reduce nonspecific binding, the coverslip was coated with a BSA-biotin-streptavidin layer. First, the silicone well was filled with 9 μl of PBS. Next, 1 μl of biotinylated BSA stock solution (10 mg/ml BSA-biotin in a buffer containing 10 mM Tris-HCl and 100 mM NaCl at pH 8.0, stored in 20-μl aliquots at $-20\,^{\circ}$C) was added and mixed by resuspension with a pipette. The solution was left to incubate for 2 minutes to allow the BSA to attach to the glass. Free-floating BSA-biotin was then

removed through 10 cycles of washing: 5 μl of solution was removed and replaced with 5 μl of PBS, mixing thoroughly after each cycle. This process was repeated with the streptavidin stock solution (10 mg/ml streptavidin in the same buffer, stored in 10-μl aliquots at $-20\,^{\circ}$C). Specifically, 5 μl of the solution in the well was removed and replaced with 5 μl of the streptavidin stock. The solution was incubated for 2 minutes and then washed using the same cycle as before. The buffer used for both stock solutions consists of 10 mM Tris-HCl and 100 mM NaCl at pH 8.0 and can be stored at room temperature for up to 6 months.

Step 5: DNA Origamis

The DNA origamis were prepared in aliquots at a concentration of 33.7 ng/μl, with each DNA origami weighing approximately 4.5 MDa. To dilute the sample, 1 μl of the Origami concentrate was dissolved in 100 μl PBS, reducing the concentration by a factor of 100. This solution was further dissolved by a factor of 100 using PBS. Subsequently, 1 μl of this dilution was added to the well, achieving a final reduction in concentration by a factor of 10^5. The origamis were incubated for 10 minutes, followed by the same washing process described previously. The fluorescent channel was used as a control to verify the origami density in the field of view, as each Origami was labeled with an Alexa Fluor 647 dye.

3.3 Data analysis

For data analysis, we recommend using the open source python-based package PiSCAT, introduced in 2022 by Mirzaalian Dastjerdi et al. [12]. It is specifically designed for iSCAT data analysis, is tailored for high efficiency, and comes with useful tools such as particle detection.

3.3.1 Noise correction

Building on the noise considerations discussed in Section 2.2.2, this section outlines specific data analysis techniques aimed at improving image quality for enhanced detection of PSFs of small particles.
To counteract intensity fluctuations in the illumination light, we apply the **power normalization** function of PiSCAT. This is how it works: The power P_i for each frame i is calculated by summing all pixel values within that frame.

$$P_i = \sum_{x,y} I_i(x, y), \tag{3.4}$$

where $I_i(x, y)$ is the intensity of each pixel (x, y) at frame i. Then, the average power $\overline{P}$ across all frames is computed:

$$\overline{P}_i = \frac{1}{N} \sum_{i=1}^{N} P_i. \tag{3.5}$$

To normalize each frame, each pixel intensity in the frame is divided by the frame's power and multiplied by the average power to maintain the overall intensity scale:

$$I_i^{\text{norm}}(x, y) = I_i(x, y) \cdot \frac{\overline{P}}{P_i}. \tag{3.6}$$

The power fluctuations are calculated using $\frac{P_i}{\overline{P}} - 1$. Figure 3.6 illustrates the power fluctuations observed during an exemplary GNP DNA Origami measurement, which are below 1 %.

Next, we can apply dark frame correction. When blocking the laser light, the camera

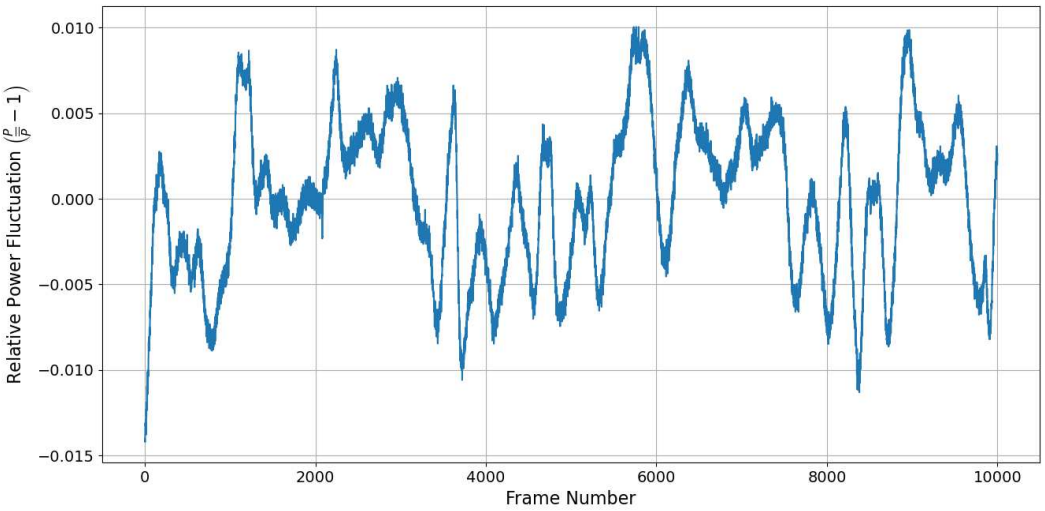

Figure 3.6: **Relative intensity fluctuations of laser in example measurement.** The 12-bit CMOS camera was set to 184 fps, leading to a total measuring length of 54 seconds.

still has an average pixel value of about 275, which is approximately 7% of the upper bound of 4069. The mean pixel value of a dark frame measurement at 184 fps is shown in Figure 3.7. Subtracting the mean pixel value of the dark frame from the measurement reduces background inhomogeneities and improves the contrast of the PSF. This correction does not reduce dark noise, which is negligible in our setup given the large well depth of 200,000 e- and the resulting shot noise in the range of 100–400 e-.

Each measurement is accompanied by a certain amount of background artifacts, which

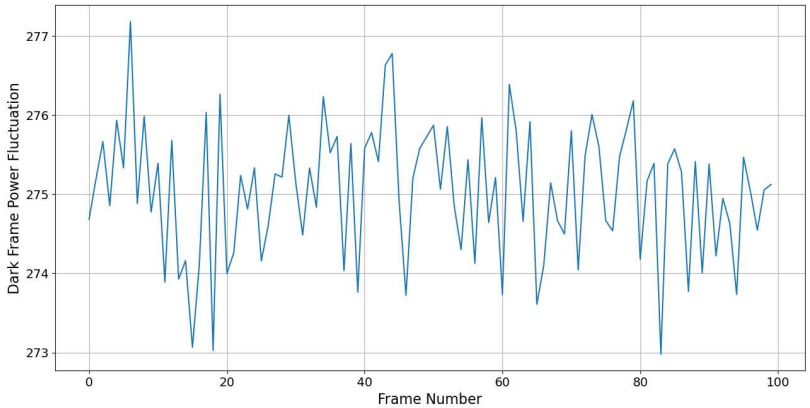

Figure 3.7: **Average pixel value of dark frame measurement.** The 12-bit CMOS camera was set to 184 fps.

can arise from factors such as the roughness of the coverslip, the illumination pattern, dust in the optical setup, or immobilized GNPs. When measuring moving particles, **differential imaging** is a powerful technique to mitigate static noise [12], [50]. PiSCAT implements this method using a rolling differential average (RDA). Figure 3.8 illustrates the effect of differential imaging over a single frame, demonstrating a significant reduction in static noise.
Differential imaging also provides information about the direction of particle movement. Depending on the axial focus, a white center in the PSF indicates a particle entering at a certain focus (e.g., moving toward the coverslip), while a black center indicates movement away from a certain focus.
Fixed pattern noise (FPN) refers to the weak stripes visible on the left in Figure 3.9.

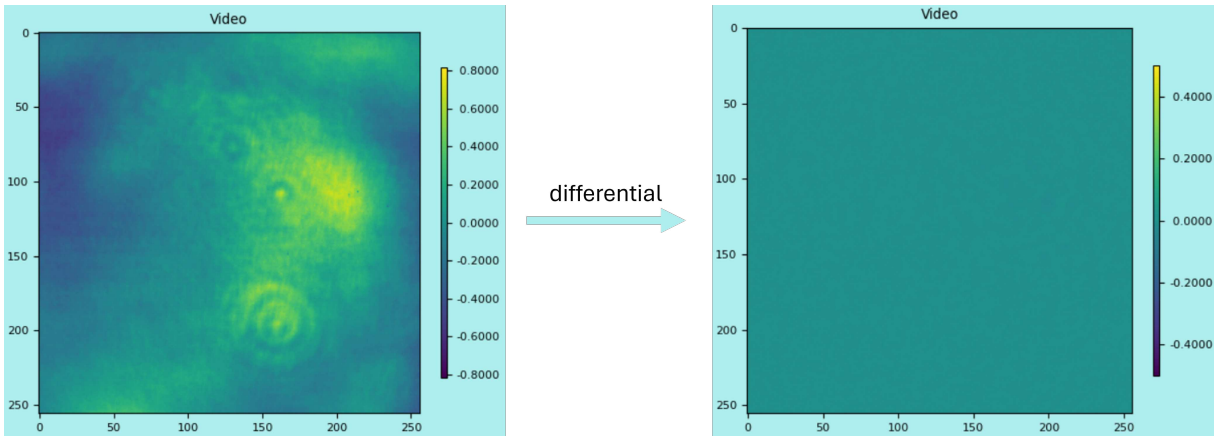

Figure 3.8: **Non differential and differential image of of iSCAT measurement.**

This artifact arises from the architecture of modern CMOS cameras designed to improve readout speed. Since FPN is not constant over time, differential imaging does not effectively eliminate it. Instead, the differential frame is processed by calculating the median of each row. This allows us to create a FPN noise map where all pixels in a given row are set to the median value of each row. The resulting noise map can then be subtracted from the image to improve the image quality. [12]

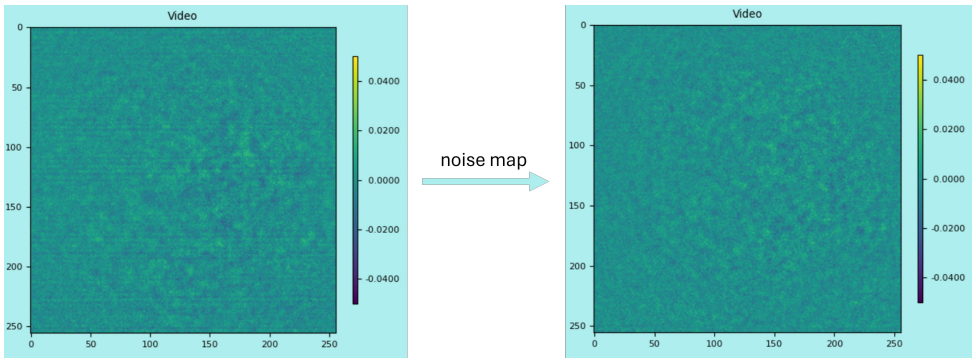

Figure 3.9: **FPN filtering using a noise map.**

To reduce spatially periodic noise, we utilize **Fourier transformation filtering**. The process begins by converting the image from the spatial domain into the frequency domain with a 2D fast Fourier transformation. Low frequencies correspond to broad, smooth

variations, while high frequencies correspond to finer details. We apply a bandpass filter in the frequency domain to filter out the interference patterns of the back reflections that we could not remove through slight misalignment of the setup, as well as filtering out other higher frequencies that arise through vibrations of the setup. Then, the filtered frequency image is transformed back into the spatial domain. An example of this frequency filtering is shown in Figure 3.10.

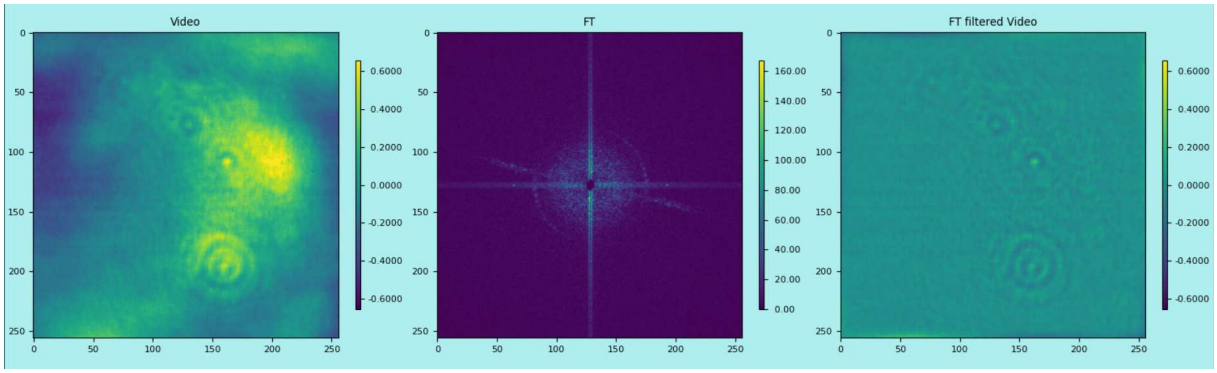

Figure 3.10: **Fourier transformation filtering.** The left image shows the unfiltered image, the center shows the frequency domain with applied bandpass filter and the right is the Fourier filter image.

Automatic particle detection is crucial when analyzing large amounts of data. To roughly detect the location of the center of the PSFs, we use the Difference of Gaussian (DoG) algorithm. The DoG algorithm works by applying two Gaussian blurs to the image, one with a small sigma (light blur - preserving smaller features) and one with a large sigma (stronger blur - smoothing out finer details). By subtracting the two blurred images, the algorithm highlights regions where the intensity changes significantly across different spatial scales. These highlighted regions are potential events of interest, such as particles.
To reduce false detections, we apply several filters:

- **Minimum sigma:** This filter excludes very small blobs, avoiding noise from tiny artifacts.
- **Maximum sigma:** This excludes large blobs, focusing on features that match the expected particle size.
- **Threshold:** This filter removes low-contrast detections, improving specificity.

The sigma value in DoG blob detection represents the standard deviation of the Gaussian filter used to blur the image. Larger sigma values correspond to detecting larger blobs, while smaller sigma values highlight finer details. By choosing the right range of sigma values, we can focus on the structures of interest while suppressing noise and irrelevant features. However, while the DoG method is effective for approximate localization, it does not achieve subpixel accuracy, which is addressed by subsequent Gaussian fitting, which will be discussed below.

Subpixel accuracy through Gauss fitting

The *photonfocus* camera has a pixel size of $10.6\,\mu\text{m} \times 10.6\,\mu\text{m}$. The magnification of the setup is the combined magnification of the objective and the 4f-system. The total magnification is calculated as the product of the objective magnification ($60\times$) and the 4f-system magnification ($\frac{200}{75}$), resulting in a combined magnification of 160. This means one pixel represents an area of $(66.25\,\text{nm})^2$. Given our objective of quantifying structures with dimensions smaller than 60 nanometers, achieving subpixel precision becomes imperative. We achieve this by fitting a 2D Gaussian over the PSF and using the center of that Gaussian as the center position of the event. This principle is illustrated in Figure 3.11.

For fitting the Gaussian on our PSF, we utilize the library/function `from scipy.optimize import curve_fit`. First, we define a simple 2D Gaussian function:

```
def gaus_2d(X, Y, b, A, xc, yc, sig):
    return b + A * np.exp(-(((X - xc) ** 2 / (sig ** 2)) + ((Y -
        yc) ** 2 / (sig ** 2))))
```

Next, we define a helper function to be inserted into our curve fitting process:

```
#: Helper Function for Gaussian Fitting
def _gaus(M, *args):
    x, y = M
    arr = np.zeros(x.shape)
    for i in range(len(args)//5):
        arr += gaus_2d(x, y, *args[i*5:i*5+5])
    return arr
```

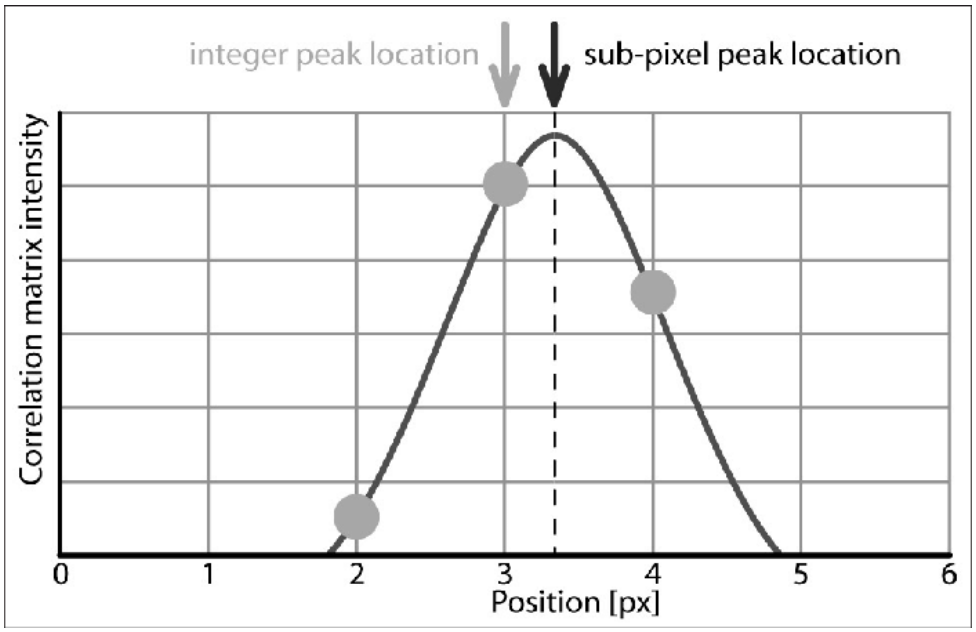

Figure 3.11: This figure, taken from [51], illustrates the principle of subpixel accuracy by fitting a 1D Gaussian over a discrete intensity distribution.

Finally, we perform the curve fitting procedure and extract the optimal parameters (`popt`) and the covariance matrix (`pcov`) by applying the curve fitting function to our data:

```
popt, pcov = curve_fit(_gaus, xdata, Z.ravel(), p0)
```

Here, `xdata` represents the x-coordinate data, `Z` represents the matrix of the observed values, and `p0` contains the initial guess values for the parameters of the Gaussian function. We obtain the guessing values for the parameters of the Gaussian function using the following approach: We use the mean value of the filtered image to provide an initial estimate for the baseline offset. To approximate the position, standard derivation and intensity values of our PSFs, we utilize the `skimage.feature.blob_dog` function. This function, part of the `skimage` library, offers preliminary x and y coordinates as well as intensity values and the standard deviation, which we can then employ as initial guessing values.

3.4 DLS

3.4.1 The DynaPro Nanostar DLS

We used the instrument DynaPro for our gold aggregation measurements. The DynaPro is a combination of DLS and Static Light Scattering (SLS). The SLS detector of the NanoStar instrument is not relevant for our measurements because it is optimized for analyzing proteins rather than gold nanoparticles. A block-diagram of the key components of the NanoStar instrument is shown in Figure 3.12. A 658 nm laser illuminates a sample sitting in a cuvette. The DLS detector is positioned at a 90-degree angle to accurately measure the size distribution of the hydrodynamic radius. It converts the photons to electrical pulses and sends them to a high-speed multi-tau correlator, which efficiently calculates the autocorrelation function over multiple timescales by using logarithmically

spaced time delays. This allows for accurate characterization of particle motion over a broad range of time intervals in real time. For weakly scattering samples, maximum laser power and minimal fiber attenuation are used to achieve optimal sensitivity. Conversely, for strongly scattering samples, attenuation is applied to prevent the detector from becoming saturated.

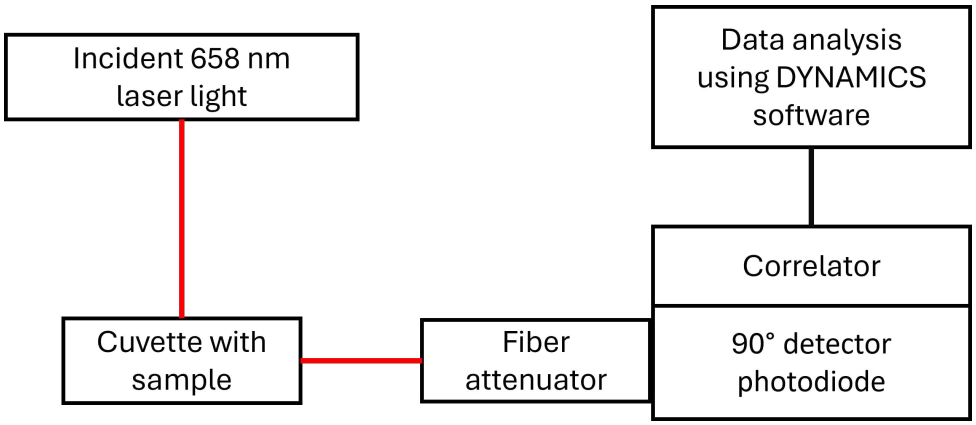

Figure 3.12: DynaPro NanoStar block diagram.

3.4.2 Conducting DLS Measurements

Cuvette Cleaning

Light scattering measurements are highly sensitive to the presence of dust and/or impurities in the sample solution. Particularly gold aggregates can stick to the quartz cuvette. Therefore, it is crucial to ensure that the light scattering cuvette is clean and free of dust before each measurement. We applied the following cleaning procedure:

1. Rinse the cuvette sequentially, first with ethanol, then with deionized water, and repeat this process once more.
2. Dry the interior of the cuvette with filtered dry compressed air.
3. Check the exterior of the cuvette for any fingerprints or smudges and remove with a piece of lens paper if necessary

Note that only high-purity ethanol should be used, as lower purity ethanol may leave stains on the cuvette. Washing the cuvette thoroughly is extra important since the GNPs tend to stick to the quartz glass. After the first few washing procedures, we recommend to conduct a measurement of the buffer solution to see if any aggregates have remained despite the washing.

Buffer conditions measured

In our experiments, each GNP is functionalized with 251 ssDNAs, each consisting of 7 base pairs. This functionalization leads to a Zeta potential of -21 mV, making the GNPs highly responsive to their environment. The attachment of DNA molecules to GNPs

significantly alters their behavior, as the Debye length of the DNA depends on the concentration of counterions in the solvent.

The valency of cations plays a crucial role: divalent ions such as Mg^{2+}, which stabilize DNA origamis, can enhance aggregation due to their ability to neutralize DNA's negative charges and possible bridging effects. Meanwhile, monovalent cations like Na^{+} have a weaker neutralizing effect. The interplay between Na^{+} and Mg^{2+} concentrations can significantly alter the structure and stability of ssDNA [48], [36]. The pH level of the buffer further influences ssDNA by affecting the protonation state of nucleotide bases, altering the overall charge and stability of the DNA-GNP system. Painting a complete picture of how different ions affect functionalized GNPs would go beyond the scope of this thesis. However, we aim to experimentally determine buffer conditions that minimize GNP aggregation to facilitate measurements of the DNA Origamis.

DLS Measurement protocol

First, we clean the cuvette. We pipetted 18 μl of the sample into the quartz cuvette, being careful to not introduce any air-bubbles. We set the temperature of the DLS instrument to 25 °C. After placing the cuvette into the instrument we wait for about half a minute to ensure that the temperature and the laser intensity are stable. Further instructions can be found in the DynaPro NanoStar User's Guide [10].

Chapter 4

Results and Discussion

4.1 Detection of GNPs

4.1.1 Simulation of contrast

The most important parameter for distinguishing GNPs from other particles, such as dust or gold aggregates, is contrast. To determine this contrast, we ran a simulation using the toolbox Nanobem from [20]. We input the approximate parameters of our setup into the Nanobem toolbox. These parameters included the refractive index of the coverslip (1.5), the refractive index of the PBS buffer (≈ 1.33), the illumination wavelength (465 nm), the GNP diameter (20 nm), the material properties of the GNP, and the numerical aperture (NA = 1.42) of the objective. The result of the simulated PSF and its corresponding vertical central intensity is shown in Figure 4.1. The Nanobem toolbox calculated a contrast value of about 8 % for the PSF of a 20 nm GNP under the discussed measuring conditions. This provides a benchmark for identifying GNPs based on their contrast relative to other particles, such as aggregates or dust, in the iSCAT images.

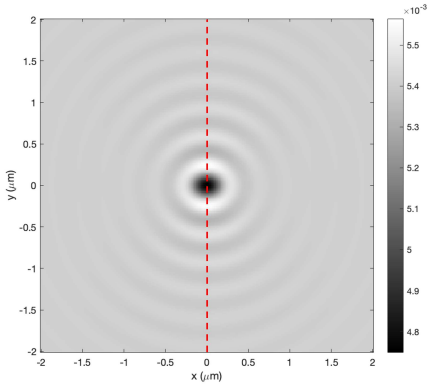

(a) PSF of Nanobem simulation.

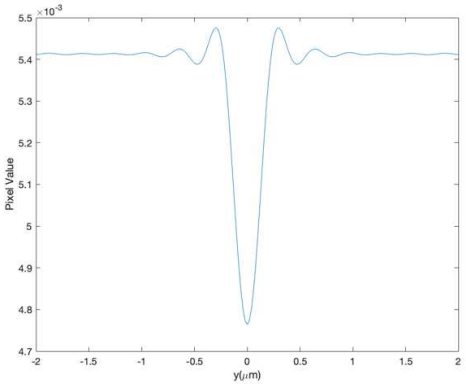

(b) Plot of central intensity of Nanobem simulation.

Figure 4.1: Figure a) shows the PSF calculated using the Nanobem toolbox [[20]]. The red dotted line indicates the column of pixels whose intensity values are plotted in b).

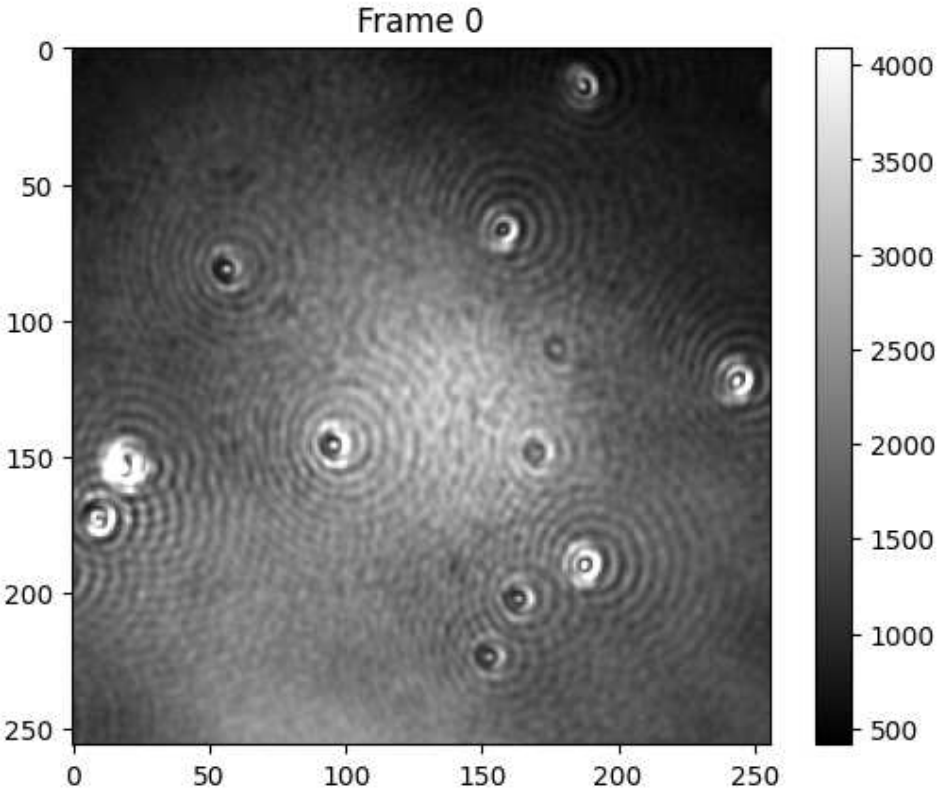

Figure 4.2: Non-differential image of an iSCAT measurement showing static 80 nm GNPs on the coverslip. The lower-contrast PSFs are likely due to dust residues.

4.1.2 Detection of the 20 nm GNPs with iSCAT

We performed measurements using the setup described in Section 3.1 to evaluate its capability to detect 20 nm GNPs. The laser intensity at the output of the optical fiber in the iSCAT path was approximately 50 mW ($\lambda = 488$ nm). As a reference, we first applied 10 μM of unfunctionalized 80 nm GNPs, dissolved in Milli-Q water, and allowed them to dry on the coverslip. These larger GNPs provided focal reference points. image Subsequently, we introduced 0.36 nM of 20 nm functionalized GNPs in PBS. The Photonfocus camera was set to an exposure time of 5 ms, as this filled the well depth of the camera without causing overexposure. Each measurement consisted of 5000 recorded frames. Figure 4.2 shows a non-differential image of the measurement. The static 80 nm GNPs are clearly visible, while the 20 nm GNPs are not, as their contrast is too low to be detected without differential imaging.

Data processing was performed using Piscat, applying the Fixed-Pattern Noise Correction Filter (fFPNc). This filter addresses fixed-pattern noise by generating a noise map through median pixel value calculations along each row or column of the image. By subtracting this noise map from the original data, the filter effectively removes consistent noise patterns, such as vertical or horizontal stripes, caused by variations in the CMOS sensor's pixel response. The fFPNc filter can dynamically update the noise map across frames, maintaining image quality even under changing conditions. When combined with differential imaging techniques, this approach significantly enhances the contrast of the PSF by reducing systematic noise. To further minimize noise, we determined the optimal batch size for frame processing using a method from [35], as illustrated in Figure 4.3.

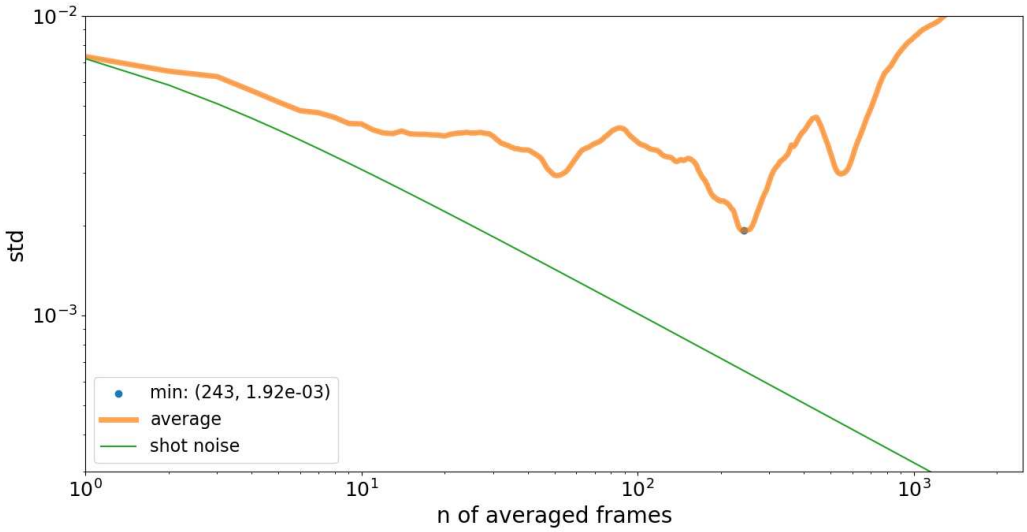

Figure 4.3: Example calculation of the differential standard deviation of an iSCAT measurement described in Section 4.1.2. The calculation was performed based on [35]. The x axis denotes the number of frames averaged and the y axis the differential standard deviation. The orange line represents the calculation of the differential standard deviation from a measurement performed as described in 4.1.2. The green line represents shot noise, which decreases with the number of averaged frames. The minimum differential standard deviation was found to be $1.92 \cdot 10^{-3}$ at $n = 243$.

The minimum standard deviation of pixel values was achieved with a batch size of 243 and was found to be $1.92 \cdot 10^{-3}$. This could be improved further by minimizing back reflection effects (see [35] and other sources of noise such as vibration introduced by the surroundings. However, PSFs with a contrast of 8 % remain detectable at this noise level. Two example frames with applied filters are shown in Figure 4.4. The 20 nm GNPs were detectable only when they landed on the glass coverslip. Following the introduction of 20 nm GNPs, numerous binding events were observed. Contrast determination was performed via Gaussian fitting using the method described in Section 3.3.1. The contrast for the PSFs marked by the red arrows were found to be at around 1 %. The lower contrast is likely due to the PSFs of the 20 nm GNPs being out of focus, reducing their contrast, despite the 80 nm GNPs being well-focused.
This effect can be attributed to the sensitivity of axial displacement inherent to iSCAT: when a particle shifts by only a quarter of the illumination wavelength (in our case $\frac{\lambda}{4} \approx 116$ nm), the scattered light undergoes a phase shift of $\frac{\pi}{2}$ relative to the reference field, altering the interference pattern in the iSCAT image. This means that even slight focus variations can have a significant affect on the signal - for example, focusing at the top or bottom of an 80 nm GNP. In our measurements, focusing was performed manually and by eye. Future measurements should aim to improve focus precision to focus on the PSFs of the 20 nm GNPs. Nevertheless, the observed PSFs appeared only after introducing the 20 nm GNPs, supporting their identification despite the reduced contrast.

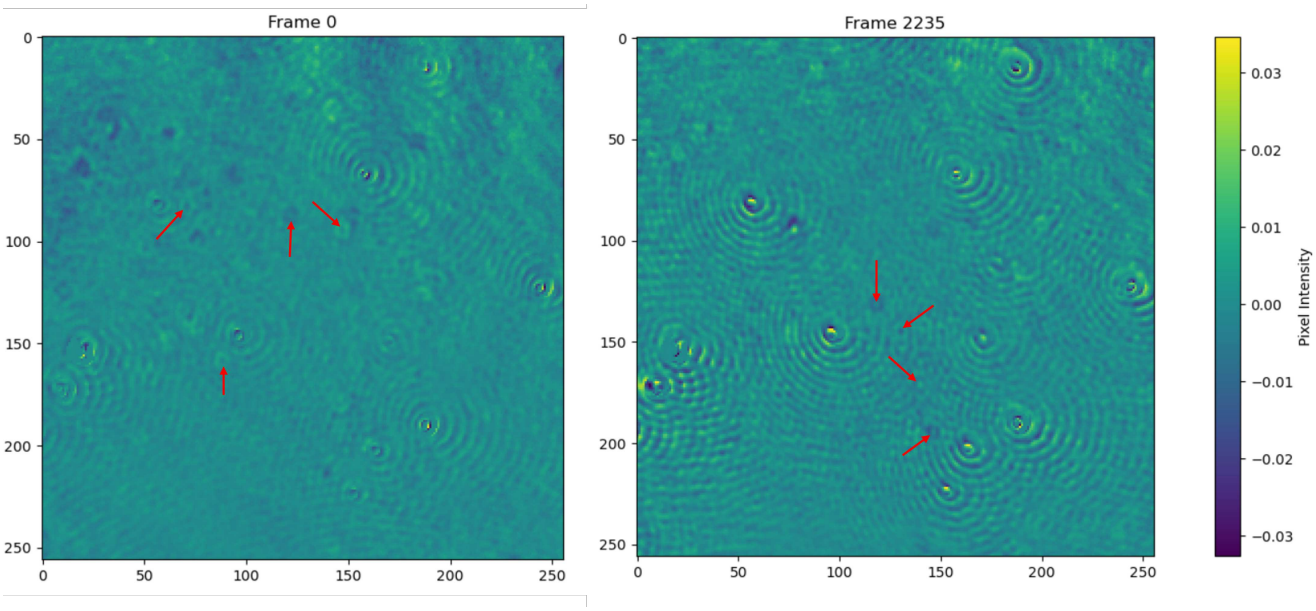

Figure 4.4: Two example frames from an iSCAT measurement performed as described in Section 4.1.2. Although out of focus, the PSFs of the 20 nm functionalized GNPs arriving on the coverslip remain visible, with four examples marked by red arrows in each frame. The more pronounced PSFs likely originate from larger structures, such as dust particles or GNP aggregates.

4.2 Synthesis of DNA Origami

4.2.1 DNA-PAINT measurement

To verify successful synthesis and folding of the DNA Origami structures, we performed DNA-PAINT measurements using established protocols (see Section 6.3). The measurements were carried out in standard folding buffer (12.5 mM $MgCl_2$, 10 mM Tris, and 10 mM EDTA at pH 8.0), which provides ideal conditions for maintaining Origami integrity. The fluorescent dye ATTO655 was chosen due to its brightness, photostability, and compatibility with DNA-PAINT.

Figure 4.5 shows the result of one such measurement. The four corners of the rectangular DNA Origami are clearly visible, indicating successful folding and the presence of functional docking sites. This confirms that the DNA Origami structures are intact and capable of interacting with imager strands as expected.

While the expected dimensions of the structure are approximately 40 nm by 60 nm, the observed shape in this image appears slightly smaller and distorted, measuring closer to 30 nm by 50 nm. This deviation can likely be attributed to several factors. First, DNA origamis do not always lie perfectly flat on the coverslip surface; they can adopt a range of orientations, including tilted or even nearly vertical configurations. In such cases, the projected shape onto the imaging plane may appear as a rhomboid rather than a rectangle, leading to apparent compression of the measured dimensions. Second, the functionalized surface itself is not perfectly smooth: it may contain nanoscale valleys and elevations that affect the local orientation of the origamis. Additionally, due to limited experience at the time of this measurement, the accuracy of corner localization and dimension annotation was suboptimal. With current expertise, this analysis could be improved significantly.

Nevertheless, the distinct visibility of all four corners remains the key result. It demonstrates that the DNA Origami structures were successfully synthesized, properly folded, and functional in the context of DNA-PAINT.

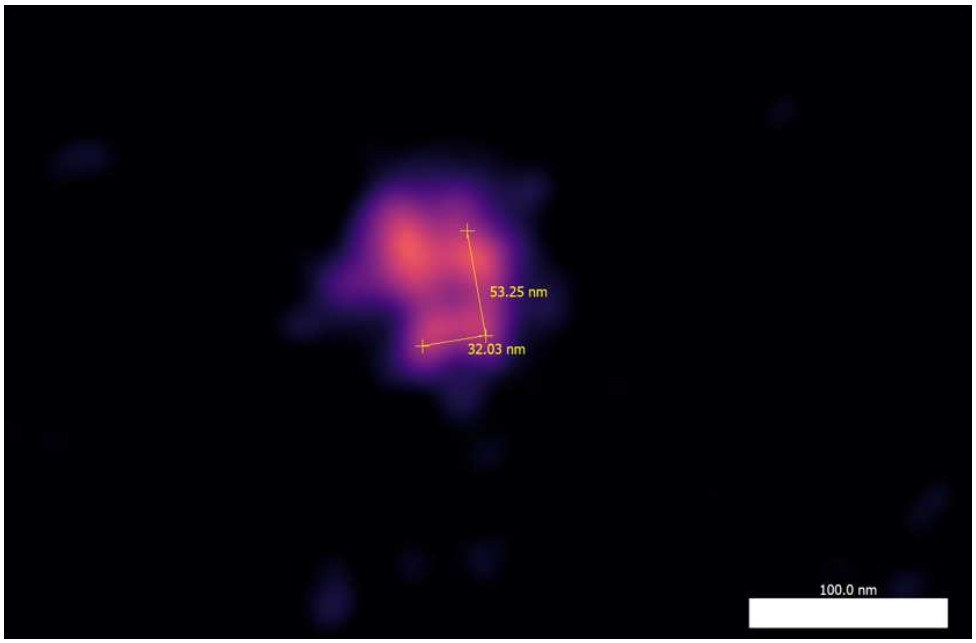

Figure 4.5: DNA-PAINT image of the four corners of a rectangular DNA Origami structure.

4.2.2 DNA Origami Stability

We aim to control the chemical environment of the DNA Origami to prevent GNP aggregation and to influence the binding lifetime of the GNPs to the Origami's docking strands. Managing different ion concentrations and pH levels are crucial strategies to achieve this control. Especially high Mg2+ concentrations lead to GNP aggregation. At the same time, DNA origamis are known to be less stable in environments with low Mg2+ ($\leq$1 mM) [23]. We conducted an agarose gel electrophoresis test to analyze DNA Origami stability in different buffers. Find the protocol on how to run the gel electrophoresis test in section 6.3.2. We prepared nine samples to evaluate DNA Origami stability under a range of conditions:

(a) DNA Origami scaffold

(b) Origami in 1x folding Buffer (12.5 mM $MgCl_2$, 100 mM Tris, 10 mM EDTA at pH8)). This is the perfect environment for DNA Origami and acts as the positive control.

(c) We exposed the Origami to 70 °C in 1x folding buffer, to ensure deformations as the negative control.

(d) DNA Origami in Milli-Q water

(e) DNA Origami in PBS pH 5

(f) DNA Origami in PBS pH 6

(g) DNA Origami in PBS pH 7.3

(h) DNA Origami in PBS pH 8

(i) DNA Origami in PBS + 1 mM MgCl1

The gel analysis results are presented in Figure 4.6, plotted using the Fiji software. The program aligns the signals using the ladder as a reference, allowing us to analyze the gray value relative to the direction of sample migration. Figure 4.7 displays the analysis, where the x-axis represents the position in the migration direction, and the y-axis denotes pixel intensity.
Most curves peak at positions similar to the positive control, indicating proper folding, with two notable exceptions. First, the scaffold curve shows a later peak, signifying that the scaffold migrated faster through the gel. This behavior reflects the fact that DNA migration speed in agarose gel is influenced not only by molecular weight and charge but also by shape.
The negative control, represented by the red curve in Figure 4.7, exhibits three significant peaks. The central peak, though lower in intensity, aligns with the other peaks, suggesting that a significant proportion of structures retained their shape despite exposure to 70°C for one hour. A second, broader, and less intense peak, appearing as a "smear" in Figure 4.6, is located closer to the wells. This smear represents misformed Origami structures that, due to their varying shapes, migrate at different speeds through the gel. Lastly, there is a peak significantly shifted in the direction of migration, corresponding to faster-moving structures. These represent staples that detached from the Origami during the heating process.
The well-defined nature of the curves for samples in Milli-Q water and PBS buffers across pH levels 5–8 indicates that the Origami structures remain stable across the various buffer conditions tested even at low Mg2+ concentrations.

4.3 Results of the DLS measurements

This section will present the results of the DLS measurements conducted to assess GNP aggregation in various buffer solutions. To understand GNP aggregation, we tested GNPs in buffers containing various ions at different concentrations. This allows us to predict and control aggregation. We studied NaCl, a common buffer component, and KCl, an essential cellular ion [52]. For the divalent ions, we examined Mg2+, crucial for DNA Origami stability (see section 4.2.2), and Zn2+, which has a higher electronegativity than Mg2+, predicting stronger GNP aggregation. Additionally, we assessed the influence different pH levels on GNP aggregation, and compared results with unfunctionalized GNPs for NaCl and $MgCl_2$. We analyzed 20 nm functionalized GNP aggregation across NaCl, KCl, $MgCl_2$, and $ZnCl_2$ concentration gradients, and various pH levels using PBS buffers. In one experiment, we introduced 20 mM $MgCl_2$ to PBS buffers with varying pH levels to observe pH impacts on aggregation. We also evaluated the level of aggregation of 20 nm citrate-stabilized GNP without DNA functionalization in NaCl and $MgCl_2$. We will call these GNPs "unfunctionalized GNPs" meaning the GNPs are not functionalized with DNA. However, it is impossible to create GNPs without any kind of functionalization, as the high surface energy of gold and attractive Van der Vaals interactions between the metal cores would lead to irreversible aggregation [14]. All experiments used a GNP concentration of 0.7 nM, consistent with iSCAT measurements. Samples were freshly

prepared on the day of measurement to ensure accuracy and consistency. The temperature was set to 25 °C.

Error of Sample preparation

Variability in sample preparation can arise from differences in preparation time, temperature, and slight variations in GNP and ion concentrations. Additionally, the composition of PBS buffers may vary slightly between batches. This section aims to quantify the error arising from sample preparation. We prepared five samples with 0.7 nM GNPs in PBS with 20 mM $MgCl_2$ at different times (hours apart), using different PBS buffers, and different pipettes for all concentrations. The resulting autocorrelation curves, along with the mean and the standard deviation, are shown in Figure 4.8. Compared to the error of the DLS measuring device discussed below, the variability of the sample preparation can be neglected in the following discussion.

Instrument error

For each measurement, the *NanoPro* DLS instrument takes ten individual acquisitions that are then averaged. Each acquisition was set to five seconds. The evaluation of the single autocorrelation curves of the acquisitions allows us to evaluate the measuring error of the setup. An example measurement can be seen in Figure 4.9. One can see that the error is considerably higher than the error of sample preparation.

Effect of Various Salts on Functionalized GNP Aggregation

First, we performed Dynamic Light Scattering (DLS) measurements on 0.7 nM functionalized GNPs in Milli-Q water. NaCl was gradually introduced until a concentration of 1 M was reached, exceeding the concentrations anticipated for DNA Origami measurements. The results are presented in Figure 4.10. Using DYNAMICS software, we calculated the hydrodynamic radius from the autocorrelation functions, averaging through all concentrations at 11.6 ± 0.4 nm (root mean square error). The ACFs show minimal shifts, indicating that the functionalized GNPs remain stable and do not aggregate at NaCl concentrations up to 1 M.

Next, we explored the effect of different KCl, $MgCl_2$, and $ZnCl_2$ concentrations on the aggregation, as shown in Figure 4.11c. The buffer used was Milli-Q water. The KCl does not induce any measurable clumping of the functionalized GNPs at concentrations of 1 M and below, with an average hydrodynamic radius at 11.6 ± 0.3 nm for all concentrations, similar to the NaCl measurements.

In contrast, the ACFs for $MgCl_2$ started shifting to the right, indicating higher aggregation, between concentrations of 10 mM and 20 mM. This suggests that functionalized GNPs are more sensitive to aggregate with $MgCl_2$ compared to NaCl. For $ZnCl_2$, aggregation of the functionalized GNPs began at concentrations between 500 μM and 1 mM. This is more visually evident in Figure 4.12, which compares the average hydrodynamic radii of the GNP aggregates at different $MgCl_2$ and $ZnCl_2$ concentrations.

Unfunctionalized GNPs

We repeated the DLS measurements for the NaCl and $MgCl_2$ concentration ramps with citrate-stabilized GNPs with 20 nm diameter without DNA functionalization, making it possible to assess if the DNA functionalization leads to more or less aggregation. The results of NaCl can be seen in Figure 4.13. We notice that the unfunctionalized GNPs start clumping between 100 mM and 250 mM NaCl as the ACFs are shifted to the right. At 500 mM NaCl there are effectively no single GNPs detected. These results indicate that DNA functionalization significantly enhances the stability of GNPs by reducing aggregation under high salt concentrations.
This statement was confirmed when measuring the unfunctionalized GNPs with a $MgCl_2$ concentration ramp, shown in Figure 4.14. The unfunctionalized GNPs start aggregating at approximately 2.5 mM, while the functionalized GNPs start aggregating only at a concentration between 10 and 20 mM. This is more visually evident in Figure 4.15, which compares the average hydrodynamic radii of the unfunctionalized and functionalized GNP aggregates at different $MgCl_2$ concentrations.

pH Level

We investigated the influence of varying pH levels on the aggregation of functionalized GNPs. PBS buffers with pH levels ranging from 4 to 10 were prepared by adding hydrochloric acid (HCl) or sodium hydroxide (NaOH), respectively. The results are shown in Figure 4.16a. Within this pH range, no aggregation was detected, with an average hydrodynamic radius of 11.3 ± 0.17 nm.
Next, we examined functionalized GNPs in PBS at pH levels from 4 to 8, with the addition of 20 mM $MgCl_2$ to induce aggregation. This allowed us to study the effect of pH on aggregated GNPs. The results are shown in Figure 4.16b. We observed decreased aggregation with lower pH levels, with no significant aggregation detected at pH 5 and below, where the average hydrodynamic radius was 12.8 nm.

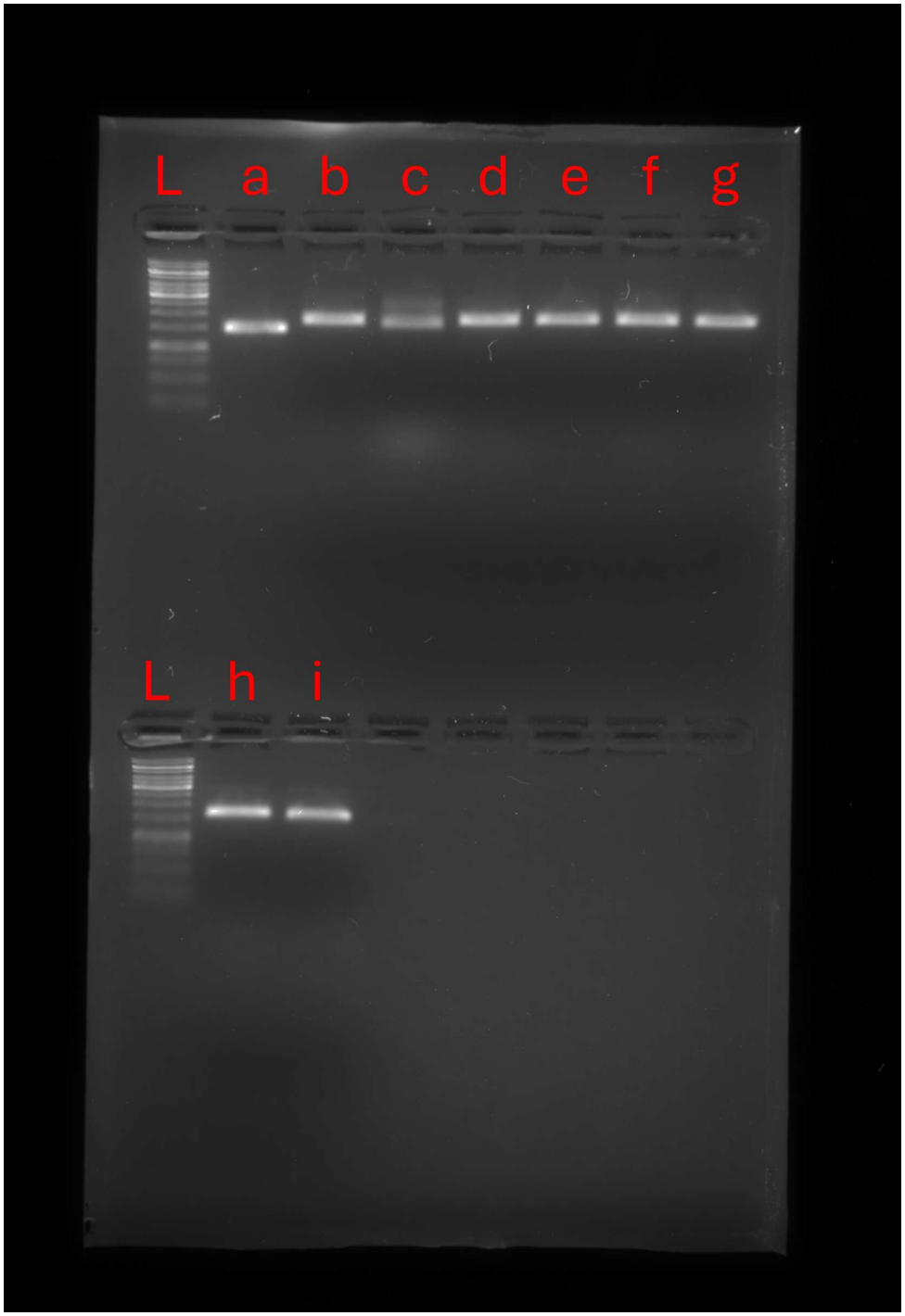

Figure 4.6: **Gel electrophoresis analysis of DNA origamis subjected to various chemical environments to assess stability.** Lane L contains the DNA Ladder for reference. Lane a: Scaffold (unfolded DNA Origami). Lane b: DNA Origami in 1x Folding buffer (positive control). Lane c: DNA Origami in 1x Folding buffer heated to 70°C for 1 hour (negative control). Lane d: DNA Origami in milliQ water. Lane e: DNA Origami in PBS pH 5. Lane f: DNA Origami in PBS pH 6. Lane g: DNA Origami in PBS pH 7.3. Lane h: DNA Origami in PBS pH 8. Lane i: DNA Origami in PBS with 1 mM MgCl2. The stability of the DNA Origami is indicated by the presence of distinct bands corresponding to the intact structures in lanes b, d, e, f, g, h, and i, while lane c shows a smear indicating deformation of the DNA Origami structure, indicating structural deformation.

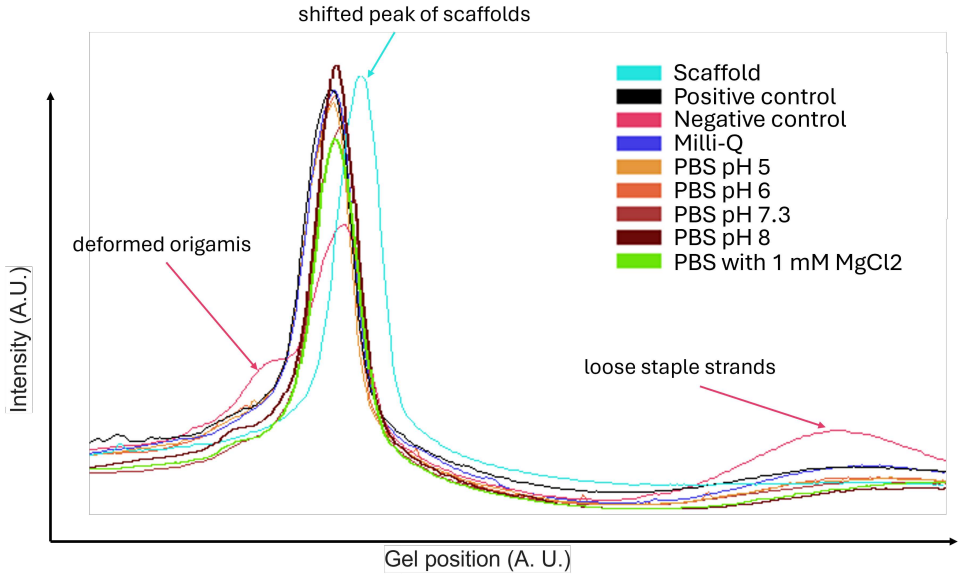

Figure 4.7: **Pixel intensity as a function of gel migration position for DNA origamis in different buffer conditions.**

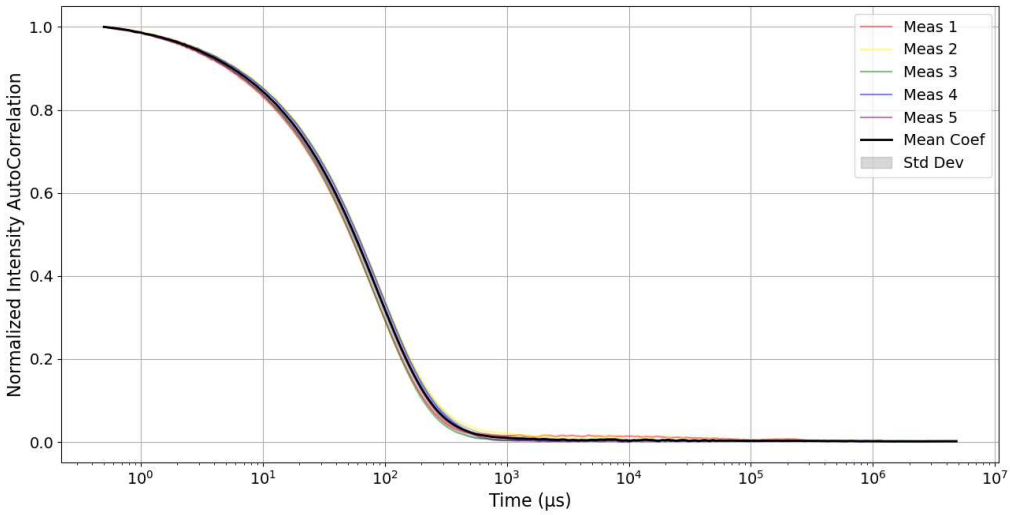

Figure 4.8: **Error of Sample Preparation**: Five measurements of the same sample prepared at different times and with different equipment. Their mean is shown in black and the standard deviation in gray. Each measurement consists of 10 acquisitions.

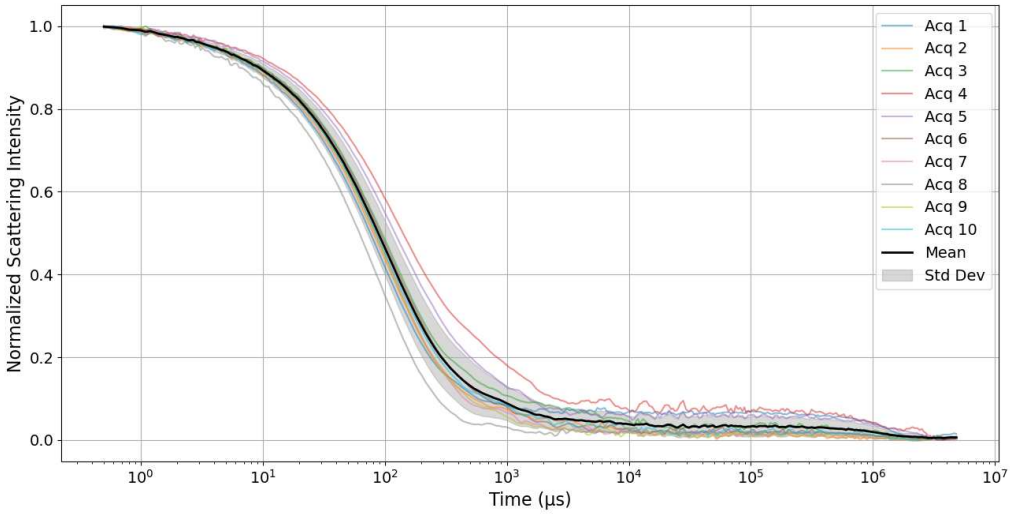

Figure 4.9: **Error of Acquisitions**. Example measurement of 0.7 nM functionalized GNPs in PBS and 20 mM $MgCl_2$. Using the 10 Acquisitions, the mean and standard deviation is calculated. The mean is shown in black and the standard deviation in grey.

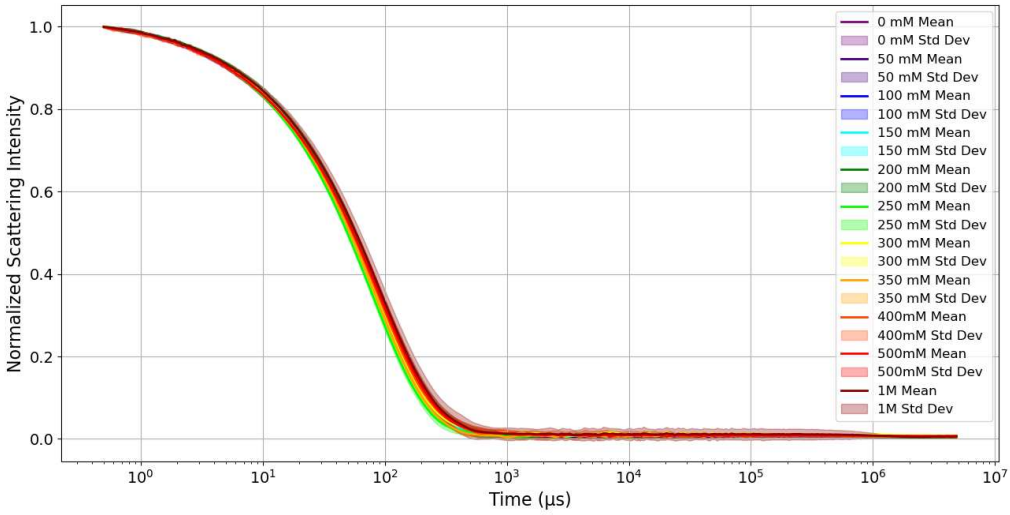

Figure 4.10: **DLS measurement of functionalized GNPs in varying NaCl concentrations.** The error was calculated by the standard deviation of the ten acquisitions as discussed in section 4.3.

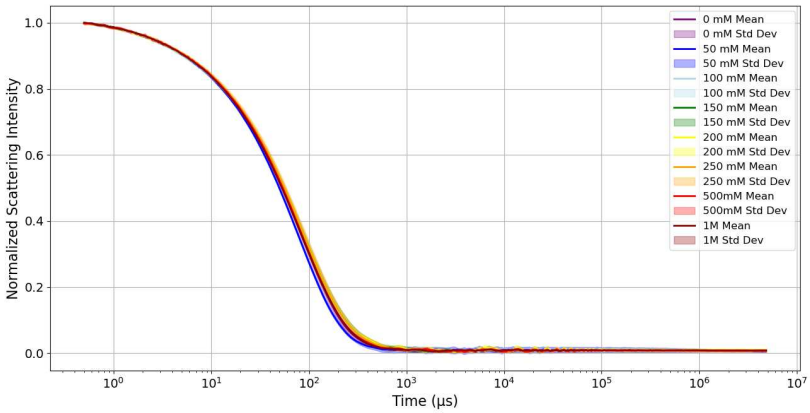

(a) Varying KCl concentrations

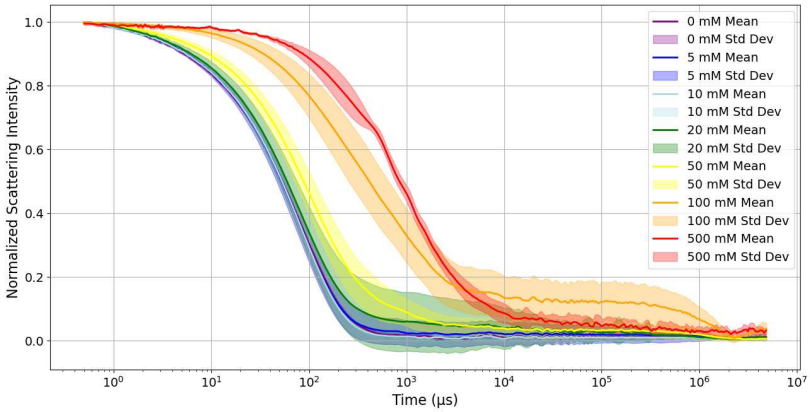

(b) Varying $MgCl_2$ concentrations

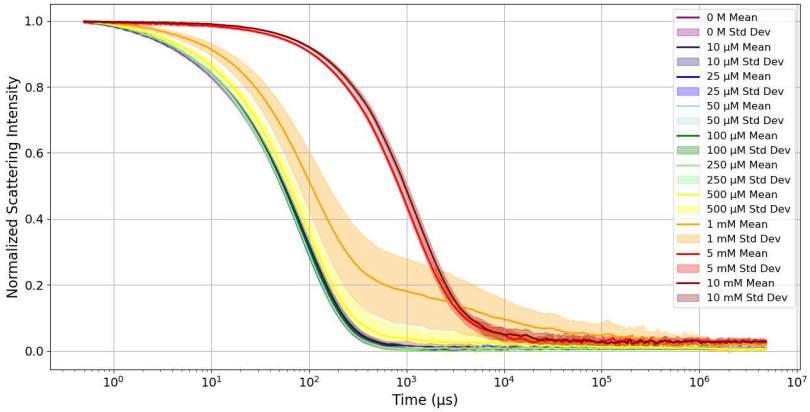

(c) Varying $ZnCl_2$ concentrations

Figure 4.11: **DLS measurement of functionalized GNPs in different varying ion concentrations.**

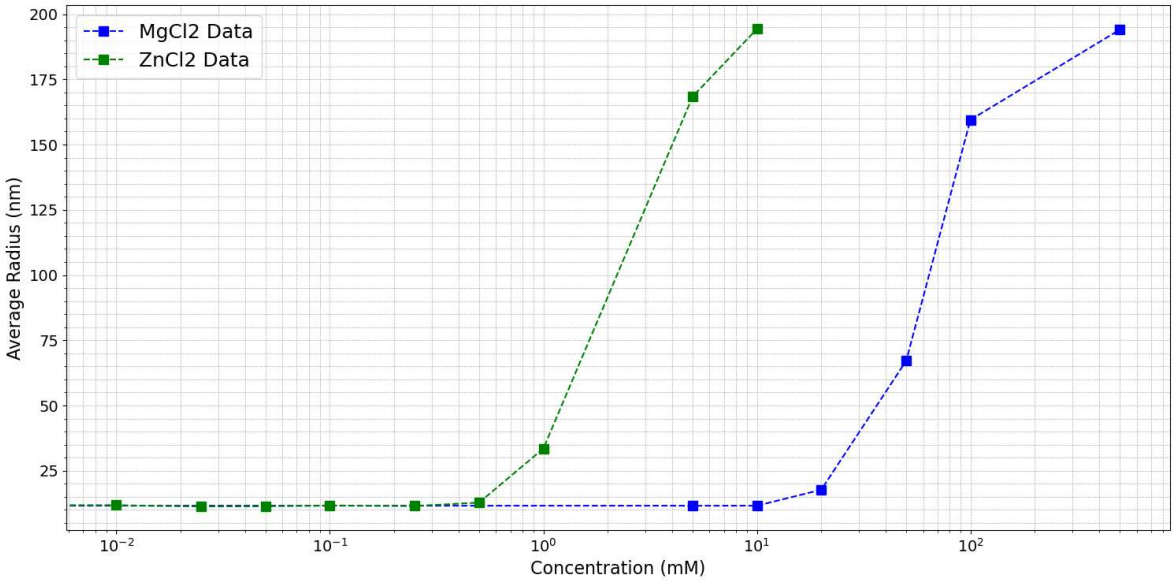

Figure 4.12: **Average hydrodynamic radius of functionalized GNPs at different $MgCl_2$ (blue) and $ZnCl_2$ (green) concentrations**. The GNPs exhibit aggregation at $ZnCl_2$ concentrations of 1 mM and above, whereas aggregation in response to $MgCl_2$ occurs only at approximately 20 mM. This demonstrates a markedly higher sensitivity of the GNPs to $ZnCl_2$-induced aggregation compared to $MgCl_2$.

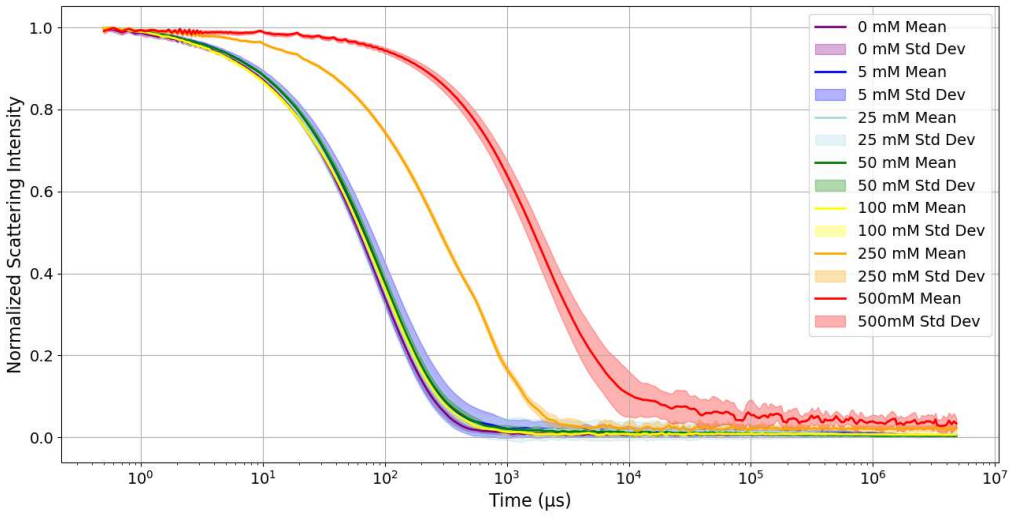

Figure 4.13: **DLS measurement of unfunctionalized GNPs in varying NaCl concentrations.** The error was calculated by the standard deviation of the ten acquisitions as discussed in section 4.3.

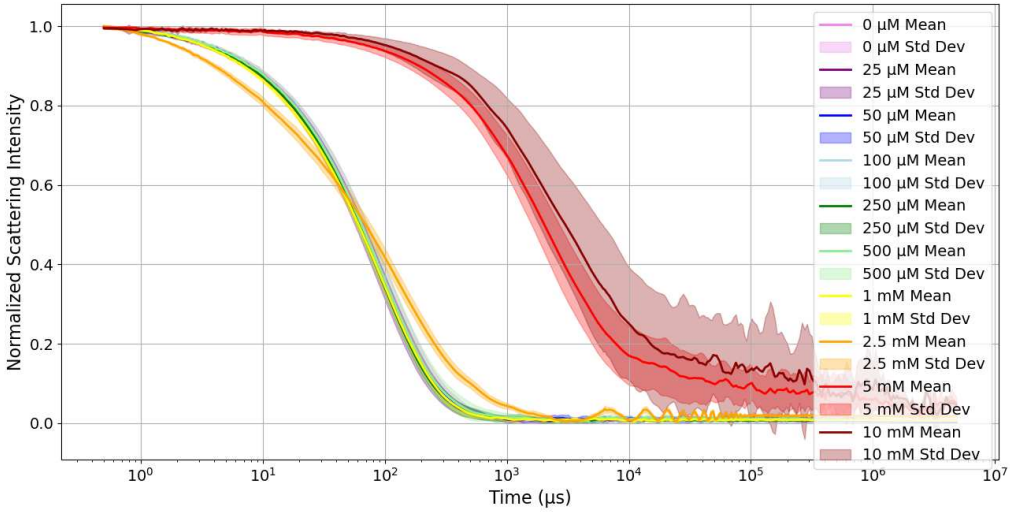

Figure 4.14: **DLS measurement of unfunctionalized GNPs in varying $MgCl_2$ concentrations.** The error was calculated by the standard deviation of the ten acquisitions as discussed in section 4.3.

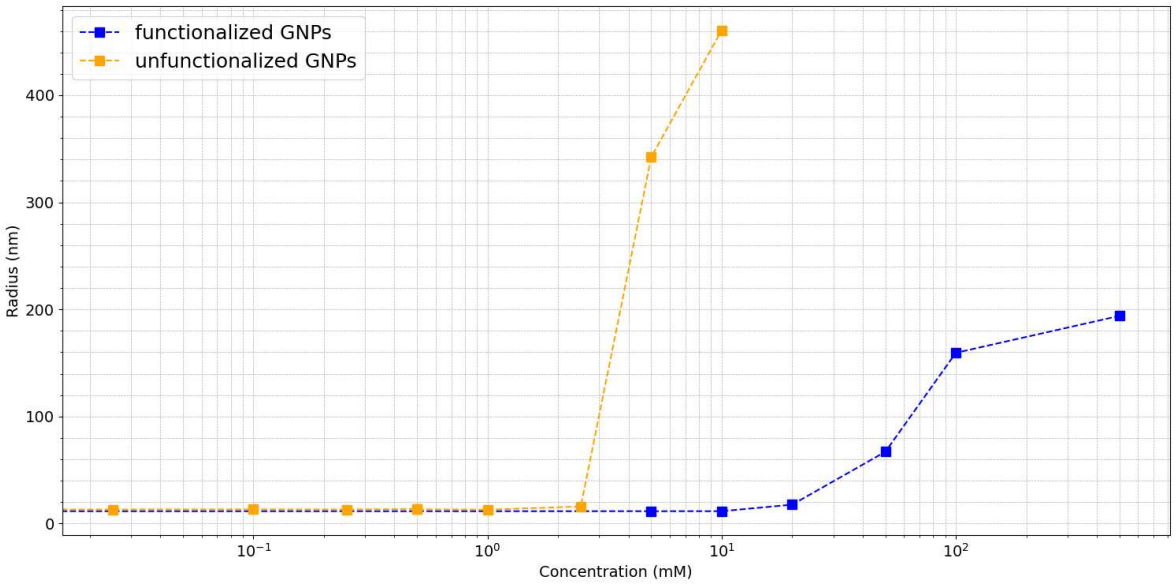

Figure 4.15: **Average hydrodynamic radius of functionalized GNPs (blue) and unfunctionalized GNPs (orange) at different $MgCl_2$ concentrations**. Unfunctionalized GNPs begin to aggregate at $MgCl_2$ concentrations exceeding 2.5 mM, whereas functionalized GNPs remain stable until approximately 20 mM. This indicates that the functionalization effectively enhances resistance to aggregation.

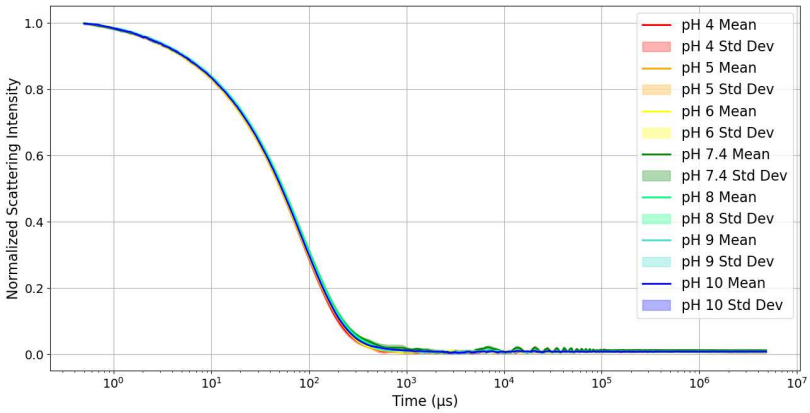

(a) GNPs in PBS

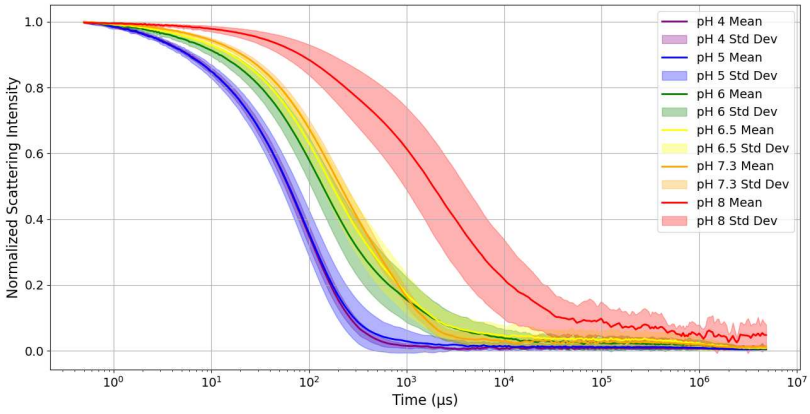

(b) GNPs in PBS with 20 mM $MgCl_2$

Figure 4.16: **DLS measurement of functionalized GNPs at varying pH level.**

4.4 Effects of Ion Concentrations on GNP Aggregation

In this section, we discuss the results of the DLS measurements presented earlier. We aim to understand the optimal conditions for using functionalized GNPs in iSCAT DNA-PAINT measurements and to identify the limiting conditions for future measurements in less controllable environments, such as living cells. More specifically, we want to prevent GNPs from forming aggregates, as aggregates sink to the coverslip quickly due to their weight, reducing the concentration of gold particles. This leads to less binding of GNPs to the corners of the DNA origamis and thus to less information. Furthermore, bigger gold aggregates introduce a large amount of noise, since they scatter light very efficiently. This leads to problems in particle detection since unwanted events will be detected, making automated particle detection near impossible.

Counterions and Aggregation

Firstly, we observed that in general, higher concentrations of counterions lead to more aggregation. The pH level measurements in PBS with 20 mM $MgCl_2$ constitute an exception and will be discussed below. Bare GNPs are inherently hydrophobic, which can lead to strong aggregation in aqueous solutions. To mitigate this, GNPs are functionalized with hydrophilic molecules to enhance their solubility. In our case, we use covalent polymer bridges with DNA as the functionalizing agent, which introduces a hydrophilic character and a negative charge on the GNP surface, promoting electrostatic repulsion and thus reducing aggregation. However, the addition of counterions to the solution can neutralize the negative charges on the DNA-functionalized GNPs. This reduction in surface charge diminishes the electrostatic repulsion between nanoparticles, thereby decreasing their hydrophilicity. Consequently, the nanoparticles are more prone to aggregation, as the neutralization of charges makes aggregation energetically favorable.

Monovalent and Divalent Ions

DLS measurements revealed that divalent ions induce significantly stronger aggregation of GNPs compared to monovalent ions. This outcome aligns with expectations, as divalent ions carry twice the charge of monovalent ions. However, in experiments with functionalized GNPs, the monovalent ions don't lead to aggregation at concentrations of up to 1 M, whereas divalent ions such as zinc (Zn^{2+}) at 500 μM and magnesium (Mg^{2+}) at 10 mM resulted in visible aggregation (see Figure 4.12). This pronounced sensitivity suggests that factors beyond mere charge neutralization are at play, such as ion bridging. Regardless, if the use of divalent ions is unavoidable in the sample environment, it is important to keep the concentrations as low as possible to mitigate aggregation.

Zinc vs. Magnesium

Another observation is that zinc causes aggregation for concentrations more than an order of magnitude lower compared to magnesium. This phenomenon may be attributed to the higher electronegativity of zinc (1.65 on Pauling scale) compared to magnesium (1.31 on Pauling scale), leading to stronger binding interactions with the GNPs and a more

effective neutralization of the negative charges of the DNA, promoting aggregation.

Efficiency of DNA Functionalization

Important to note is that citrate-stabilized GNPs without DNA functionalization, aggregated considerably more, indicating that DNA functionalization is effective at preventing aggregation. Therefore, increasing the oligonucleotide density per GNP will likely enhance solubility of the GNPs, as each particle has a higher negative charge. This suggests that increasing the base number of each oligo by adding a linker such as poly A or poly G and to increase the oligo number per nanoparticle could be efficient strategies to prevent aggregation response to higher counterion concentrations. Since counterions like $MgCl_2$ play an important role in controlling the binding lifetime of DNA, maintaining flexibility in the selection of counterion concentration is advantageous. A potential disadvantage of increasing the length of a linker is that this might lead to a reduction in spatial resolution. However, DNA experiments with docking strands of 19 nucleotides have still managed sufficient resolution to resolve DNA origami that have similar structures to this project [47].

Effect of pH Levels

Changing the pH level between 4 and 10 in PBS did not affect aggregation of functionalized GNPs. However, when introducing 20 mM magnesium to the PBS, lower pH levels helped counteract aggregation, while higher pH levels increased aggregation. This outcome was unexpected, as lower pH implies more counterions. A possible explanation is that hydrogen ions partially shield the GNPs from the magnesium ions, reducing their likelihood of bridging. If magnesium concentrations become necessary, one could profit from a more acidic buffer solution to mitigate the aggregation effects of the magnesium. Additionally, other anti-aggregation compounds, such as EDTA, could be explored in future studies.

4.5 GNP adsorption on glass surfaces

Another challenge, particularly during longer measurements, is the adsorption of GNPs onto the coverslip surface. This phenomenon introduces additional noise, as adhered GNPs create inhomogeneities on the surface, leading to irregular scattering patterns and reducing measurement accuracy. Some adsorbed GNP aggregates are not completely static; instead, they can oscillate within a confined region, increasing the false detection rate and further contributing to noise. Additionally, the adsorption of GNPs reduces the concentration of free GNPs available to bind with DNA origamis, impairing detection performance and limiting experimental precision.
An example of GNP adsorption after two hours of measurement is shown in Figure 4.17. Future work could explore the application of anti-adsorption coatings, such as polyethylene glycol (PEG) treatments, to minimize GNP binding to glass surfaces and enhance experimental reproducibility.

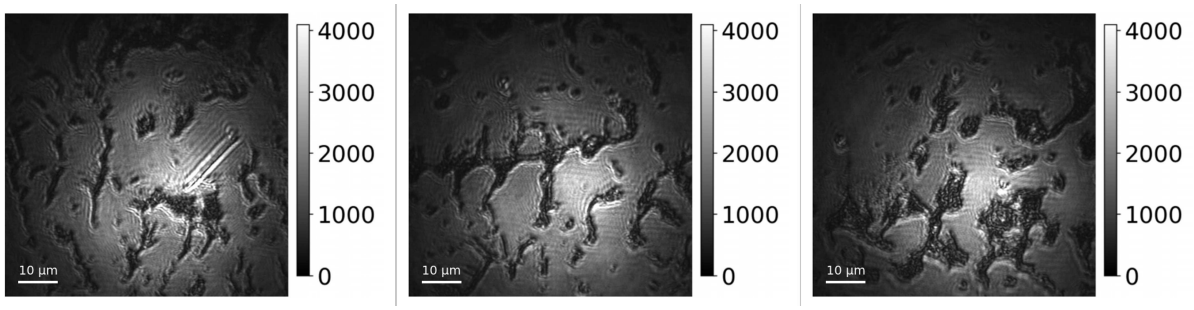

Figure 4.17: Fouling of GNPs after 2 hours of measurements. The images are non-differential and show different areas on the coverslip. The images are taken with the iSCAT setup discussed in section 3.1.

Chapter 5

Summary and Outlook

5.1 Summary

This thesis introduced the concept of combining DNA PAINT with iSCAT to achieve highly sensitive, super resolution detection of nanostructures using elastically scattering labels. The primary goal was to demonstrate the feasibility of detecting a 40 by 60 nm DNA origami structure functionalized with transiently binding 20 nm GNPs.

1. **Microscope setup:** We built a combined iSCAT and fluorescence microscope capable of alternating between modalities. This setup allowed for simultaneous validation of DNA origami structures using fluorescence and high-sensitivity detection of GNPs via iSCAT.

2. **DNA origami design and validation:** We built rectangular DNA origami structures with four docking sites as a well-defined test system. Successful folding and functionality were confirmed through DNA-PAINT measurements with fluorescent labels (ATTO655), revealing the expected geometry of the origami. Gel electrophoresis confirmed the stability of the origami under varying buffer conditions (pH 4–8, $MgCl_2$ concentrations), showing no significant degradation even at low Mg^{+2} levels.

3. **Gold nanoparticle functionalization and detection:** We functionalized 20 nm GNPs with complementary ssDNA sequences to enable transient binding to the origami docking sites. Nanobem simulations predicted an 8% contrast for 20 nm GNPs under the experimental conditions. Despite noise and system limitations, these particles were successfully detected, albeit with reduced contrast due to focus challenges.

4. **Dynamic Light Scattering characterized GNP aggregation under various buffer conditions:** For monovalent ions (NaCl, KCl) we observed no aggregation up to concentrations of 1 M. For divalent ions ($MgCl_2$, $ZnCl_2$) aggregation began at 10 mM $MgCl_2$ and 500 μM $ZnCl_2$, highlighting the GNPs higher sensitivity to divalent ions. Unfunctionalized GNPs aggregated at lower concentrations (100 mM NaCl, 2.5 mM $MgCl_2$), demonstrating the stabilizing effect of ssDNA functionalization. At 20 mM $MgCl_2$, lower pH ($\leq$5) mitigated aggregation, while higher pH increased it, suggesting a shielding effect of H^+ ions.

5. **Data analysis:** The PiSCAT software package was employed for noise reduction and particle detection, utilizing techniques such as Differential rolling average to enhance dynamic signals and remove signal from static sources, Fourier filtering to reduce periodic noise, Fixed-pattern noise correction to improve image quality.

The study successfully laid the groundwork for combining DNA-PAINT with iSCAT, demonstrating the potential for super-resolution imaging with elastic scattering labels. While challenges remain in optimizing signal-to-noise ratios and minimizing aggregation, the results highlight the promise of this approach for applications requiring high temporal and axial resolution, such as live-cell imaging or single-molecule tracking.

5.2 Outlook

The goal of this thesis was to establish the conditions necessary for a proof-of-principle detection of the 40 × 60 nm corners of the DNA origami. However, there are still several obstacles preventing the detection of DNA origamis. The aim of this section is to discuss what is to be done in the future to conduct the proof of principle DNA origami detection by combining iSCAT with DNA-PAINT. As presented in section 4.1, we successfully detected GNPs of a diameter of 20 nm. A pending issue is to increase efficiency of the GNP detection.

5.2.1 Tailor spatial coherence

The overlapping of scattering fields produce a speckle like background that make it more challenging to decipher GNPs from the background. This effect is particularly important in iSCAT PAINT, where the high number of scattering sources increases the background noise. Furthermore, the higher orders of the PSFs, especially those caused by GNP aggregates, create concentric ring-like structures in the field of view that lead to false detection by the difference of Gaussian blob detection method (see section 4.1). Thus, reducing the amount of PSF rings, can help to reduce the number of false detections.
Reducing the spatial coherence of the illumination, as demonstrated by [30], has been shown to suppress speckle patterns and reduce the number of false positives. By placing a rotating diffuser coupled to an adjustable lens and an iris in the illumination path, the amount of visible higher order rings of the PSFs is suppressed leading to less false positive detections through reduction in speckles and less rings created by aggregates.

5.2.2 Algorithm for GNP detection

So far, for particle detection, a simple DoG blob algorithm has been implemented. The ratio of false to true positives may be improved by exploring more sophisticated PSF detection algorithms. Neural networks, in particular, have proven to be a powerful tool to reduce the number of false positives [4], and to increase the detection sensitivity [11]. A study reduced the false positive rate to 3.5 % using a mask region-based convolutional neural network, compared to 19.8 % when using a Haar-like feature image segmentation algorithm, which is already more elaborate than a simple DoG blob algorithm [4].

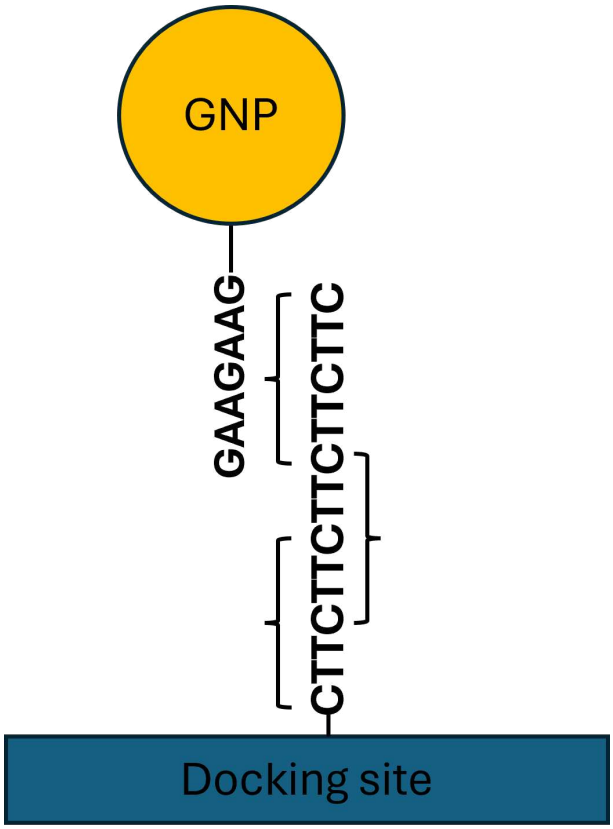

Figure 5.1: Sketch of periodic motive of docking strands. In this example, the imaging strand of the GNP has three options of hybridizing to the imaging strand.

5.3 Enhancing GNP Functionalization for Improved Performance

We tried detecting the DNA origamis using a simple DNA functionalization, namely imaging strands and the complimentary sequence as docking strands. However, there are multiple changes in this setup that can improve the association rates and reduce non-specific binding such as aggregation and fouling. Enhancing the association rate improves measurement quality by increasing the number of docking events, thereby extracting more information per label. This, in turn, enhances both the spatial and temporal resolution of the measurement.

To enhance the association rates of GNPs with DNA origami structures, the incorporation of periodic sequence motifs has been proposed. For instance, consider the imaging strand sequence GAAGAAG, which is designed to hybridize with the complementary docking site sequence CTTCTTC. By periodically extending the docking site sequence by an additional six bases, resulting in CTTCTTCTTCTTC, the imaging strand GAAGAAG is provided with three distinct sites for potential binding. The number of sequence repeats is linearly correlated with the binding frequency, thereby improving the overall association efficiency. This concept is illustrated in Figure 5.1. [41], [47]

The buffer conditions provide another lever to influence the binding frequency. More specifically, increasing the salinity of the buffer increases the binding frequency as it reduces the melting temperature of DNA. For example, increasing $MgCl_2$ concentration

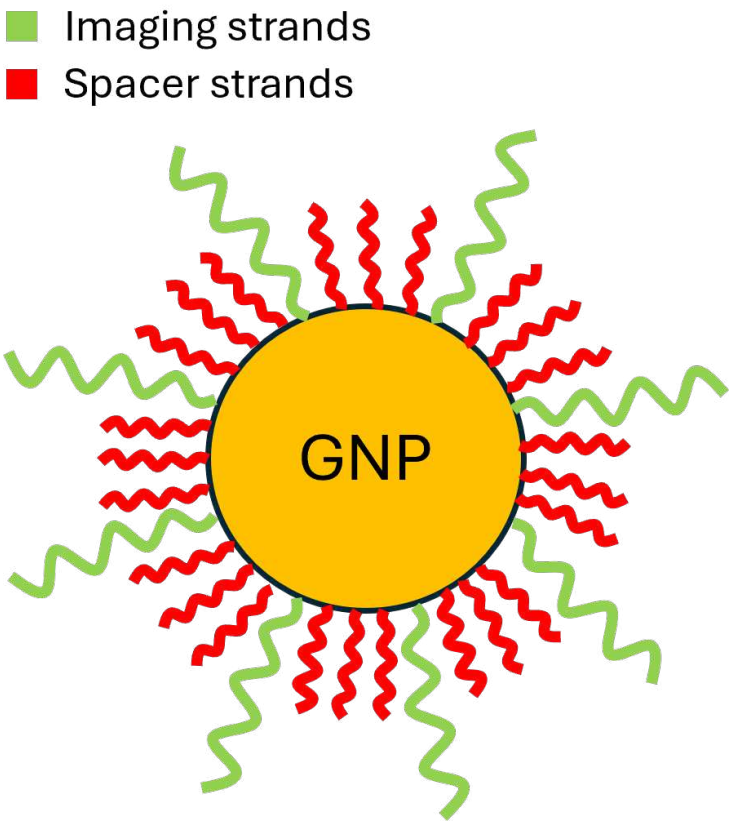

Figure 5.2: Sketch of GNP with spacer strands (red) and imaging strands (green).

from the standard 10 mM to 75 mM resulted in a two-fold speed increase in DNA-PAINT imaging [41]. However, this must be balanced by the increase in aggregation through higher ion concentration as seen in section 4.3.
Linkers play a significant role in influencing the binding properties of functionalized GNPs. Specifically, the presence of a poly-A spacer between the gold nanoparticle surface and the DNA imaging sequence is critical for enhancing binding efficiency, by moving the sequence further away from the GNP surface, thereby reducing steric hindrance allowing better hybridization with the target sequence. Adding a poly-A linker comes with the additional advantage of increasing the negative charge of the GNP, reducing aggregation. [29]
Intuitively, increasing the oligo density on the GNPs should lead to higher association rates. However, a too high density decreases surface accessibility. Adding spacer strands between the imaging strands as shown in Figure 5.2 increases surface accessibility and thus helps to increase association rates by up to 15-fold. A monolayer of spacer strands further suppresses non-specific binding and thus adsorption of the GNPs on the glass surface. [13]

5.4 Mitigating Non-Specific Binding

The GNPs sticking to the glass coverslip has been one issue as it reduces association rates and introduces higher noise levels. While adding spacer strands to the GNPs is one way to reduce non-specific binding with the coverslip, another approach is to engineer an anti-fouling coating on the coverslip. Finding an efficient and easy to implement anti-fouling

coating will be an important step to improve the measurements.

In summary, with an efficient particle detection algorithm, suppression of non-specific binding and a sufficient number of specific GNP-origami binding events, detecting the DNA origamis by combining iSCAT with DNA-PAINT is realistic.

5.5 The potential of combining DNA-PAINT with iSCAT

The combination of DNA-PAINT and iSCAT microscopy has the potential to overcome key limitations of fluorescence-based super-resolution imaging.

Using GNPs as labels is a simple alternative as GNPs scatter light almost regardless of the chemical and physical environment. This allows for measurements where little prior knowledge of the conditions is needed. The limiting factor however is the functionalization of the GNPs as the binding dynamics of DNA is influenced by the environment. Furthermore, in too high salt concentrations, especially for divalent ions, aggregation can become a problem. This too can be dealt with via improved functionalization.
Another advantage of GNPs is that they do not bleach. However, bleaching is not the primary challenge in fluorescent DNA-PAINT, as dyes are continuously replaced through the dynamic binding and unbinding of fluorescent labels. In recent years, various strategies have been developed to mitigate fluorophore bleaching and enhance imaging longevity. One such strategy is Repeat DNA-PAINT, which significantly suppresses background signals and reduces non-specific binding, thereby improving fluorophore efficiency and extending imaging durations [9]. Additionally, oxygen scavenger buffer systems [39], red-shifted dyes [24], and adaptive illumination strategies [45] have further contributed to prolonging fluorophore longevity in DNA-PAINT. As a result, measurement durations have reached the time scale of hours, with some studies demonstrating long-term DNA-PAINT imaging for up to 60 minutes [5]. However, for even longer measurement durations, the implementation of GNPs could prove beneficial.
Another advantage of elastically scattering labels is reduced photo-toxicity compared to fluorescent probes. Fluorophores dissipate absorbed energy through vibrational relaxation, in other words, the inelastic scattering process deposits heat into the local environment and generates reactive oxygen species that can damage biological samples [25]. GNPs, by contrast, undergo purely elastic scattering without energy dissipation into molecular vibrations, making them particularly suitable for imaging of delicate samples, including crowded intracellular spaces [26].

The typical DNA-PAINT temporal resolution ranges from approximately 1 second down to 100 milliseconds per localization event. For example, *Lin et al.* [28] reported a frame integration time of 100 ms, which defines the temporal resolution in their experiments. In contrast, iSCAT measurements achieve significantly higher temporal resolution. In our experiments (see 4.1), the camera exposure time was set to 5 ms. With increased laser power, even shorter exposure times are possible.
Furthermore, standard DNA-PAINT achieves an axial localization precision on the order of tens of nanometers, with one study reporting an axial resolution of 80 nm [40]. There are recent advancements in DNA-PAINT - particularly when combined with techniques

like MINFLUX [32] and graphene energy transfer (GET) [53] - that have pushed axial localization precision precision down to 0.3 nm. However, these methods are complex to implement. In contrast, iSCAT intrinsically offers high axial precision in the nanometer range, as discussed in 2.2. This higher precision could be particularly beneficial for measuring subtle axial displacements, such as the vertical motion of biomolecules, nanoscale structural changes, or surface interactions at the single-molecule level.

A key advantage of DNA-PAINT lies in its potential for highly multiplexed imaging. Early implementations, such as fluorescent DNA-PAINT, achieved multiplexing by utilizing spectrally distinct fluorophores [27]. However, the number of fluorophores that can be reliably differentiated in a single experiment is fundamentally constrained by spectral overlap and the photophysical properties of the dyes. This limitation is addressed by Exchange-PAINT, which enables virtually unlimited multiplexing by sequentially introducing dye-labeled imager strands that are orthogonal in sequence. Each imager strand binds specifically to its corresponding docking strand, which is uniquely associated with a particular biological target. After imaging one target, the imager strand is washed out and replaced with the next, thereby allowing sequential visualization of multiple targets using the same fluorophore. This sequence-based strategy eliminates the need for multiple dyes, offering high specificity and flexibility while preserving super-resolution imaging capabilities [39].
Despite its advantages, Exchange-PAINT is limited by the time-intensive nature of the sequential washing and imaging steps, particularly when a large number of targets are involved. Moreover, this approach is not suitable for live-cell imaging or for tracking dynamic biological processes in real time, as only one fluorophore can be imaged at any given moment.
GNPs offer a promising solution to these limitations due to their size-dependent optical properties. For example, consider a GNP with a radius of 10 nm, exhibiting a simulated iSCAT contrast of $C_{10} = 8\%$ (see Section 4.1.1). The contrast C_{11} for a GNP with a radius of 11 nm can be estimated using the volumetric scaling relation:

$$\frac{C_{11}}{C_{10}} = \left(\frac{11\,\text{nm}}{10\,\text{nm}}\right)^3 = 1.331 \tag{5.1}$$

Solving for C_{11} yields:

$$C_{11} = C_{10} \cdot 1.331 \approx 10.65\% \tag{5.2}$$

Given that iSCAT can achieve noise levels of 10^{-3} and even lower (see Section 4.1 and [35]), the resulting contrast difference of approximately 2.35% is well above the detection threshold and is readily distinguishable. Consequently, by employing GNPs of different sizes, each functionalized with a unique docking strand, it is possible to achieve simultaneous multiplexed imaging of multiple targets. This strategy not only enables the observation of dynamic biological processes in real time but also significantly reduces acquisition time by eliminating the need for repeated washing steps.

In summary, the combination of DNA-PAINT with iSCAT presents a promising alternative to traditional fluorescence-based super-resolution microscopy. The key advantage of iSCAT lies in its superior temporal resolution and nanometer-scale axial precision, which surpasses the capabilities of fluorescent DNA-PAINT. Moreover, the use of GNPs as labels

offers additional benefits, such as photostability, high multiplexing ability, lower phototoxicity, and reduced dependence on environmental conditions, though functionalization remains a critical factor. While fluorescence-based DNA-PAINT has seen significant advancements in mitigating bleaching and extending imaging durations, iSCAT's ability to operate without a photon budget limitation allows for exceptionally short exposure times and higher frame rates. By integrating these two techniques, iSCAT could be transformed into a super-resolution method, while DNA-PAINT could benefit from enhanced sensitivity and faster acquisition times, making this hybrid approach a powerful tool for nanoscale imaging.

Chapter 6

Appendix

6.1 Experimental setup components

This section lists the components we used in our setup. The list is an updated version taken from [35].

Component	**Model**	**Property**
old objective	Zeiss Plan-Apochromat	x63, NA = 1.4
new objective	Thermo Scientific Olympus	x60, NA = 1.42
tube lenses	Zeiss	f = 164.5 mm
beam splitter	Thorlabs Plate Beamsplitter	Non-Polarizing, 2 inch
upwards mirror	Thorlabs BBE1-E02	
mirror tip-tilt stage	Edmund Optics 66-543	
mirror translation stage	Thorlabs DT12/M	
sample x-y stage	opto-sigma TSD-1202SH-M6	
sample z stage	Thorlabs SM1ZA	
objective piezo stage	Physikinstrumente	
cover slips	Zeiss 1.5H	170 μm x 18 mm x 18 mm
4f system lens 1	Thorlabs AC508-075-A-ML	f = 75 mm
4f system lens 2	Thorlabs AC508-200-A-ML	f = 200 mm

Table 6.1: Components of the sample stage, 4f system, and objective

6.2 DNA Origami

This section will list all components of the DNA Origami used in this project. Table 6.5 lists all unmodified staple strands necessary for rectangle origami folding. Table 6.6 lists all biotinylated staple strands for rectangle origami surface attachment. The biotin comes as a 5‘ modification in all cases. Table 6.7 lists all modified DNA-PAINT handle extensions. The "Staple" means the sequence of the unmodified DNA origami

Component	Model	Property
laser	Nichia NUBM07E	λ = 465 nm, power 3500 mW
fiber incoupling lens	Thorlabs A110TM-A	f = 6.24 mm, NA = 0.40
optical fiber	Thorlabs P3-488PM-FC-1	FC/APC
outcoupling collimator	Thorlabs PAF2A-15A	f = 15.4 mm, d = 2.52 mm
camera	photonfocus MV1-D1024E-160-CL	pixel size = 10.6 μm x 10.6 μm

Table 6.2: Components of the iSCAT channel

Component	Model	Property
laser	Vortran Stradus	λ = 642 nm, power 10 - 100 mW
optical fiber	Thorlabs P3-630PM-FC-1	FC/APC
incoupling lens	Thorlabs A110TM-A	f = 6.24 mm, NA = 0.40
outcoupling objective	4X Olympus Plan Achromat	0.10 NA, 18.5 mm WD
translation stage	Thorlabs XR25C	25 mm range
correction lens	Thorlabs LA1433-A-ML	f = 150 mm
dichroic mirror	custom from an old setup	illumination incoupling
dichroic mirror	Edmund Optics 69-215	separate iScat from excitation
dichroic mirror	Edmund Optics 67-084	separate excitation from emission
long pass filter	Thorlabs FELH0650	in front of camera

Table 6.3: Components of fluorescent channel

Component	Model	Property
mirrors	Thorlabs PF10-03-P01-10	silver
posts	Thorlabs RS50/M	
mirror holders	radiant dyes mdi	for most components
mirror holders	Polaris K25S4/M	for iScat illumination
cage mounts	Thorlabs CP35	
cage translation stages	Thorlabs SM1ZA	

Table 6.4: General components

staple should be added. Finally, table 6.8 lists the fluorescently modified oligonucleotides used for DNA-PAINT in section 4.2.1 and the stably bound markers used for the DNA-Origami. The middle row shows the positional data for each staple strand following a semi-standardized notation generated by the DNA origami design software Cadnano. In this system, every staple is defined by two coordinate pairs: the first pair indicates the 5´ start position, and the second pair marks the 3´ end position of the strand. Each

coordinate consists of a helix number (outside square brackets) and a nucleotide position along that helix (inside brackets). For example, the entry 15[32]17[31] denotes a staple that begins at the 32nd nucleotide of helix 15 and ends at the 31st nucleotide of helix 17, suggesting a crossover between these two helices. This grid-based indexing ensures precise mapping of staple-scaffold interactions, which is critical for the accurate assembly of the origami structure.

Table 6.5: Supplementary Table. List of unmodified staples of DNA origamis.

Number	**Name**	**Sequence (5' → 3')**
1	23[224]22[240]	GCACAGACAATATTTTTGAATGGGGTCAGTA
2	1[128]4[128]	TGACAACTCGCTGAGGCTTGCATTATACCAAG CGCGATGATAAA
3	7[96]9[95]	TAAGAGCAAATGTTTAGACTGGATAGGAAGCC
4	11[224]13[223]	GCGAACCTCCAAGAACGGGTATGACAATAA
5	10[143]9[159]	CCAACAGGAGCGAACCAGACCGGAGCCTTTAC
6	11[32]13[31]	AACAGTTTTGTACCAAAAACATTTTATTTC
7	10[207]8[208]	ATCCCAATGAGAATTAACTGAACAGTTACCAG
8	12[207]10[208]	GTACCGCAATTCTAAGAACGCGAGTATTATTT
9	19[160]20[144]	GCAATTCACATATTCCTGATTATCAAAGTGTA
10	0[111]1[95]	TAAATGAATTTTCTGTATGGGATTAATTTCTT
11	13[64]15[63]	TATATTTTGTCATTGCCTGAGAGTGGAAGATT
12	16[207]14[208]	ACCTTTTTATTTTAGTTAATTTCATAGGGCTT
13	10[47]8[48]	CTGTAGCTTGACTATTATAGTCAGTTCATTGA
14	1[192]4[192]	GCGGATAACCTATTATTCTGAAACAGACGATT GGCCTTGAAGAGCCAC
15	18[175]16[176]	CTGAGCAAAAATTAATTACATTTTGGGTTA
16	16[47]14[48]	ACAAACGGAAAAGCCCCAAAAACACTGGAGCA
17	16[143]15[159]	GCCATCAAGCTCATTTTTTAACCACAAATCCA
18	11[256]13[255]	GCCTTAAACCAATCAATAATCGGCACGCGCCT
19	8[79]6[80]	AATACTGCCCAAAAGGAATTACGTGGCTCA
20	2[79]0[80]	CAGCGAAACTTGCTTTCGAGGTGTTGCTAA
21	13[192]15[191]	GTAAAGTAATCGCCATATTTAACAAAACTTTT
22	15[256]18[256]	GTGATAAAAAGACGCTGAGAAGAGATAACCTT GCTTCTGTTCGGGAGA
23	23[64]22[80]	AAAGCACTAAATCGGAACCCTAATCCAGTT
24	15[160]16[144]	ATCGCAAGTATGTAAATGCTGATGATAGGAAC
25	6[271]4[272]	ACCGATTGTCGGCATTTTCGGTCATAATCA
26	13[256]15[255]	GTTTATCAATATGCGTTATACAAACCGACCGT

27	13[32]15[31]	AACGCAAAATCGATGAACGGTACCGGTTGA
28	0[143]1[127]	TCTAAAGTTTTGTCGTCTTTCCAGCCGACAA
29	10[111]8[112]	TTGCTCCTTTCAAATATCGCGTTTGAGGGGGT
30	4[207]2[208]	CCACCCTCTATTCACAAACAAATACCTGCCTA
31	20[143]19[159]	AAGCCTGGTACGAGCCGGAAGCATAGATGATG
32	6[47]4[48]	TACGTTAAAGTAATCTTGACAAGAACCGAACT
33	8[239]6[240]	AAGTAAGCAGACACCACGGAATAATATTGACG
34	4[111]2[112]	GACCTGCTCTTTGACCCCCAGCGAGGGAGTTA
35	4[143]3[159]	TCATCGCCAACAAAGTACAACGGACGCCAGCA
36	3[224]5[223]	TTAAAGCCAGAGCCGCCACCCTCGACAGAA
37	21[32]23[31]	TTTTCACTCAAAGGGCGAAAAACCATCACC
38	2[143]1[159]	ATATTCGGAACCATCGCCCACGCAGAGAAGGA
39	12[47]10[48]	TAAATCGGGATTCCCAATTCTGCGATATAATG
40	6[143]5[159]	GATGGTTTGAACGAGTAGTAAATTTACCATTA
41	10[271]8[272]	ACGCTAACACCCACAAGAATTGAAAATAGC
42	9[96]11[95]	CGAAAGACTTTGATAAGAGGTCATATTTCGCA
43	23[128]23[159]	AACGTGGCGAGAAAGGAAGGGAAACCAGTAA
44	14[111]12[112]	GAGGGTAGGATTCAAAAGGGTGAGACATCCAA
45	2[239]0[240]	GCCCGTATCCGGAATAGGTGTATCAGCCCAAT
46	5[32]7[31]	CATCAAGTAAAACGAACTAACGAGTTGAGA
47	17[160]18[144]	AGAAAACAAAGAAGATGATGAAACAGGCTGCG
48	20[271]18[272]	CTCGTATTAGAAATTGCGTAGATACAGTAC
49	17[96]19[95]	GCTTTCCGATTACGCCAGCTGGCGGCTGTTTC
50	19[96]21[95]	CTGTGTGATTGCGTTGCGCTCACTAGAGTTGC
51	3[32]5[31]	AATACGTTTGAAAGAGGACAGACTGACCTT
52	4[79]2[80]	GCGCAGACAAGAGGCAAAAGAATCCCTCAG
53	1[32]3[31]	AGGCTCCAGAGGCTTTGAGGACACGGGTAA
54	1[256]4[256]	CAGGAGGTGGGGTCAGTGCCTTGAGTCTCTGA ATTTACCGGGAACCAG
55	16[175]14[176]	TATAACTAACAAAGAACGCGAGAACGCCAA
56	1[64]4[64]	TTTATCAGGACAGCATCGGAACGACACCAAC CTTAAAACGAGGTCAATC
57	6[207]4[208]	TCACCGACGCACCGTAATCAGTAGCAGAACCG
58	20[207]18[208]	GCGGAACATCTGAATAATGGAAGGTACAAAAT
59	23[192]22[208]	ACCCTTCTGACCTGAAAGCGTAAGACGCTGAG
60	3[96]5[95]	ACACTCATCCATGTTACTTAGCCGAAAGCTGC

61	21[160]22[144]	TCAATATCGAACCTCAAATATCAATTCCGAAA
62	21[248]23[255]	AGATTAGAGCCGTCAAAAAACAGAGGTGAGGC CTATTAGT
63	23[256]22[272]	CTTTAATGCGCGAACTGATAGCCCCACCAG
64	22[111]20[112]	GCCCGAGAGTCCACGCTGGTTTGCAGCTAACT
65	2[47]0[48]	ACGGCTACAAAAGGAGCCTTTAATGTGAGAAT
66	21[184]23[191]	TCAACAGTTGAAAGGAGCAAATGAAAAATCTA GAGATAGA
67	22[175]20[176]	ACCTTGCTTGGTCAGTTGGCAAAGAGCGGA
68	18[47]16[48]	CCAGGGTTGCCAGTTTGAGGGGACCCGTGGGA
69	12[143]11[159]	TTCTACTACGCGAGCTGAAAAGGTTACCGCGC
70	16[79]14[80]	GCGAGTAAAAATATTTAAATTGTTACAAAG
71	17[224]19[223]	CATAAATCTTTGAATACCAAGTGTTAGAAC
72	12[271]10[272]	TGTAGAAATCAAGATTAGTTGCTCTTACCA
73	10[175]8[176]	TTAACGTCTAACATAAAAACAGGTAACGGA
74	2[111]0[112]	AAGGCCGCTGATACCGATAGTTGCGACGTTAG
75	8[111]6[112]	AATAGTAAACACTATCATAACCCTCATTGTGA
76	8[271]6[272]	AATAGCTATCAATAGAAAATTCAACATTCA
77	7[120]9[127]	CGTTTACCAGACGACAAAGAAGTTTTGCCATA AATTCGA
78	7[160]8[144]	TTATTACGAAGAACTGGCATGATTGCGAGAGG
79	18[271]16[272]	CTTTTACAAAATCGTCGCTATTAGCGATAG
80	22[207]20[208]	AGCCAGCAATTGAGGAAGGTTATCATCATTTT
81	0[175]0[144]	TCCACAGACAGCCCTCATAGTTAGCGTAACGA
82	22[47]20[48]	CTCCAACGCAGTGAGACGG
83	0[207]1[191]	TCACCAGTACAAACTACAACGCCTAGTACCAG
84	3[160]4[144]	TTGACAGGCCACCACCAGAGCCGCGATTTGTA
85	13[128]15[127]	GAGACAGCTAGCTGATAAATTAATTTTTGT
86	14[143]13[159]	CAACCGTTTCAAATCACCATCAATTCGAGCCA
87	15[128]18[127]	TAAATCAAAATAATTCGCGTCTCGGAAACCAG GCAAAGGGAAGGG
88	5[160]6[144]	GCAAGGCCTCACCAGTAGCACCATGGGCTTGA
89	9[64]11[63]	CGGATTGCAGAGCTTAATTGCTGAAACGAGTA
90	2[271]0[272]	GTTTTAACTTAGTACCGCCACCCAGAGCCA
91	7[184]9[191]	CGTAGAAAATACATACCGAGGAAACGCAATAA GAAGCGCA
92	16[239]14[240]	GAATTTATTTAATGGTTTGAAATATTCTTACC

93	18[111]16[112]	TCTTCGCTGCACCGCTTCTGGTGCGGCCTTCC
94	0[271]1[255]	CCACCCTCATTTTCAGGGATAGCAACCGTACT
95	0[47]1[31]	AGAAAGGAACAACTAAAGGAATTCAAAAAAA
96	1[224]3[223]	GTATAGCAAACAGTTAATGCCCAATCCTCA
97	9[160]10[144]	AGAGAGAAAAAAATGAAAATAGCAAGCAAACT
98	21[56]23[63]	AGCTGATTGCCCTTCAGAGTCCACTATTAAAG GGTGCCGT
99	22[239]20[240]	TTAACACCAGCACTAACAACTAATCGTTATTA
100	7[248]9[255]	GTTTATTTTGTCACAATCTTACCGAAGCCCTT TAATATCA
101	10[239]8[240]	GCCAGTTAGAGGGTAATTGAGCGCTTTAAGAA
102	13[224]15[223]	ACAACATGCCAACGCTCAACAGTCTTCTGA
103	2[175]0[176]	TATTAAGAAGCGGGGTTTTGCTCGTAGCAT
104	12[111]10[112]	TAAATCATATAACCTGTTTAGCTAACCTTTAA
105	22[79]20[80]	TGGAACAACCGCCTGGCCCTGAGGCCCGCT
106	0[239]1[223]	AGGAACCCATGTACCGTAACACTTGATATAA
107	12[239]10[240]	CTTATCATTCCCGACTTGCGGGAGCCTAATTT
108	11[192]13[191]	TATCCGGTCTCATCGAGAACAAGCGACAAAAG
109	17[32]19[31]	TGCATCTTTCCCAGTCACGACGGCCTGCAG
110	20[239]18[240]	ATTTTAAAATCAAAATTATTTGCACGGATTCG
111	4[271]2[272]	AAATCACCTTCCAGTAAGCGTCAGTAATAA
112	18[207]16[208]	CGCGCAGATTACCTTTTTTAATGGGAGAGACT
113	8[143]7[159]	CTTTTGCAGATAAAAACCAAAATAAAGACTCC
114	11[160]12[144]	CCAATAGCTCATCGTAGGAATCATGGCATCAA
115	14[47]12[48]	AACAAGAGGGATAAAAATTTTTAGCATAAAGC
116	15[96]17[95]	ATATTTTGGCTTTCATCAACATTATCCAGCCA
117	15[224]17[223]	CCTAAATCAAAATCATAGGTCTAAACAGTA
118	16[111]14[112]	TGTAGCCATTAAAATTCGCATTAAATGCCGGA
119	4[239]2[240]	GCCTCCCTCAGAATGGAAAGCGCAGTAACAGT
120	6[175]4[176]	CAGCAAAAGGAAACGTCACCAATGAGCCGC
121	8[47]6[48]	ATCCCCCTATACCACATTCAACTAGAAAAATC
122	14[175]12[176]	CATGTAATAGAATATAAAGTACCAAGCCGT
123	6[111]4[112]	ATTACCTTTGAATAAGGCTTGCCCAAATCCGC
124	20[79]18[80]	TTCCAGTCGTAATCATGGTCATAAAAGGGG
125	9[192]11[191]	TTAGACGGCCAAATAAGAAACGATAGAAGGCT
126	19[224]21[223]	CTACCATAGTTTGAGTAACATTTAAAATAT

127	14[271]12[272]	TTAGTATCACAATAGATAAGTCCACGAGCA
128	20[111]18[112]	CACATTAAAATTGTTATCCGCTCATGCGGGCC
129	12[175]10[176]	TTTTATTTAAGCAAATCAGATATTTTTTGT
130	8[207]6[208]	AAGGAAACATAAAGGTGGCAACATTATCACCG
131	2[207]0[208]	TTTCGGAAGTGCCGTCGAGAGGGTGAGTTTCG
132	9[128]11[127]	GCTTCAATCAGGATTAGAGAGTTATTTTCA
133	7[224]9[223]	AACGCAAAGATAGCCGAACAAACCCTGAAC
134	1[160]2[144]	TTAGGATTGGCTGAGACTCCTCAATAACCGAT
135	20[175]18[176]	ATTATCATTCAATATAATCCTGACAATTAC
136	14[239]12[240]	AGTATAAAGTTCAGCTAATGCAGATGTCTTTC
137	19[32]21[31]	GTCGACTTCGGCCAACGCGCGGGGTTTTTC
138	4[47]2[48]	GACCAACTAATGCCACTACGAAGGGGGTAGCA
139	15[192]18[192]	TCAAATATAACCTCCGGCTTAGGTAACAATTT CATTTGAAGGCGAATT
140	6[239]4[240]	GAAATTATTGCCTTTAGCGTCAGACCGGAACC
141	0[79]1[63]	ACAACTTTCAACAGTTTCAGCGGATGTATCGG
142	22[143]21[159]	TCGGCAAATCCTGTTTGATGGTGGACCCTCAA
143	7[56]9[63]	ATGCAGATACATAACGGGAATCGTCATAAATA AAGCAAAG
144	15[32]17[31]	TAATCAGCGGATTGACCGTAATCGTAACCG
145	23[160]22[176]	TAAAAGGGACATTCTGGCCAACAAAGCATC
146	1[96]3[95]	AAACAGCTTTTTGCGGGATCGTCAACACTAAA
147	12[79]10[80]	AAATTAAGTTGACCATTAGATACTTTTGCG
148	23[32]22[48]	CAAATCAAGTTTTTTGGGGTCGAAACGTGGA
149	13[160]14[144]	GTAATAAGTTAGGCAGAGGCATTTATGATATT
150	21[120]23[127]	CCCAGCAGGCGAAAAATCCCTTATAAATCAA GCCGGCG
151	21[224]23[223]	CTTTAGGGCCTGCAACAGTGCCAATACGTG
152	23[96]22[112]	CCCGATTTAGAGCTTGACGGGGAAAAAGAATA
153	11[128]13[127]	TTTGGGGATAGTAGTAGCATTAAAAGGCCG
154	20[47]18[48]	TTAATGAACTAGAGGATCCCCGGGGGGTAACG
155	5[96]7[95]	TCATTCAGATGCGATTTTAAGAACAGGCATAG
156	11[96]13[95]	AATGGTCAACAGGCAAGGCAAAGAGTAATGTG
157	13[96]15[95]	TAGGTAAACTATTTTTGAGAGATCAAACGTTA
158	4[175]2[176]	CACCAGAAAGGTTGAGGCAGGTCATGAAAG

159	15[64]18[64]	GTATAAGCCAACCCGTCGGATTCTGACGACA GTATCGGCCGCAAGGCG
160	9[224]11[223]	AAAGTCACAAAATAAACAGCCAGCGTTTTA
161	18[143]17[159]	CAACTGTTGCGCCATTCGCCATTCAAACATCA
162	9[256]11[255]	GAGAGATAGAGCGTCTTTCCAGAGGTTTTGAA
163	18[79]16[80]	GATGTGCTTCAGGAAGATCGCACAATGTGA
164	14[79]12[80]	GCTATCAGAAATGCAATGCCTGAATTAGCA
165	10[79]8[80]	GATGGCTTATCAAAAAGATTAAGAGCGTCC
166	7[32]9[31]	TTTAGGACAAATGCTTTAAACAATCAGGTC
167	8[175]6[176]	ATACCCAACAGTATGTTAGCAAATTAGAGC
168	11[64]13[63]	GATTTAGTCAATAAAGCCTCAGAGAACCCTCA
169	14[207]12[208]	AATTGAGAATTCTGTCCAGACGACTAAACCAA
170	18[239]16[240]	CCTGATTGCAATATATGTGAGTGATCAATAGT
171	16[271]14[272]	CTTAGATTTAAGGCGTTAAATAAAGCCTGT
172	6[79]4[80]	TTATACCACCAAATCAACGTAACGAACGAG
173	9[32]11[31]	TTTACCCCAACATGTTTTAAATTTCCATAT
174	5[224]7[223]	TCAAGTTTCATTAAAGGTGAATATAAAAGA
175	21[96]23[95]	AGCAAGCGTAGGGTTGAGTGTTGTAGGGAGCC
176	22[271]20[272]	CAGAAGATTAGATAATACATTTGTCGACAA

Name	**Sequence (5' → 3')**
4[255]6[248]-biotin	[BIO]AGCCACCACTGTAGCGCGTTTTCAAGGGAGGGAAGGTAAA
18[255]20[248]- biotin	[BIO]AACAATAACGTAAAACAGAAATAAAAATCCTTTGCCCGAA
18[191]20[184]-biotin	[BIO]ATTCATTTTTGTTTGGATTATACTAAGAAACCACCAGAAG
18[126]20[120]-biotin	[BIO]CGATCGGCAATTCCACACAACAGGTGCCTAATGAGTG
4[63]6[56]-biotin	[BIO]ATAAGGGAACCGGATATTCATTACGTCAGGACGTTGGGAA
18[63]20[56]-biotin	[BIO]ATTAAGTTTACCGAGCTCGAATTCGGGAAACCTGTCGTGC
4[191]6[184]-biotin	[BIO]CACCCTCAGAAACCATCGATAGCATTGAGCCATTTGGGAA
4[127]6[120]-biotin	[BIO]TTGTGTCGTGACGAGAAACACCAAATTTCAACTTTAAT

Table 6.6: Supplementary Table. List of biotinylated staples of DNA origamis.

Sequences (5'→3')	Staples it substitutes
Staple + CCCTTCTTC	144, 123, 161, 114
TAAATCATATAACCTGTTTAGCTAACCTTTAA TTTCACTCCAGGAATATAAAGC	107
TTTTATTTAAGCAAATCAGATATTTTTTGTTT GTTTCTTCGGGCGTACTGAC	135

Table 6.7: Supplementary table. List of modified staple of DNA origamis

Name	**Sequences (5'→3')**	Modification
R5-ATTO655	GAAGAAG	3' ATTO 655
Im#6-AF647	CGTCAGTACGCCCGAAGAAAC	3' Alexa Fluor 647
Im#9-AF647	CGCTTTATATTCCTGGAGTGA	3' Alexa Fluor 647

Table 6.8: Supplementary table. List of fluorescently labelled oligonucleotides used.

6.3 Protocols

6.3.1 How to make the DNA Origamis

Experiment Information

This protocol is on producing the rectangular DNA origami with 40x60 nm seperated docking strands from [39].

Folding Reaction

One mix needs to be prepared, composed of 4 oligos (all 10 μl per oligo, all oligos resuspended to 100 μM in MilliQ water):

- ori_PAINT_ET_0 MM: 999, 1000, 1001, 1002

Prepare the following mixture:

Component	**Concentration of Stock**	**Volume to Add (μl)**
10x folding buffer (on my shelf)	10x	5
Scaffold 110 nM	10 nM	4.5 μl
20 nm grid, white MM	609 nM (each staple)	8.2
20 nm grid, no corners MM	12.5 μ M (each staple)	4
Biotinylated staples master mix	12.5 μM (each staple)	4
ori_PAINT_ET_0 MM	25 μ M	2
Water	N/A	22.3

Table 6.9: Folding Reaction Mixture

Final Volume: 50 μl

Thermocycler Conditions

Fold by annealing ramp in a thermocycler:

1. 80°C for 5 minutes.
2. 60°C for 3 minutes 21 seconds.
3. 60°C to 4°C in steps of 1°C per 3 minutes 21 seconds.
4. Hold at 4°C.

Set lid temperature to 105°C and the volume to 50 μl.

PEG Purification

Perform three rounds of PEG precipitation:

1. Add the same volume of PEG buffer (15% PEG-8000, 500 mM NaCl, 12.5 mM MgCl2 in 1xTE pH 8.0, stored in the fridge) to the eppendorf.
2. Centrifuge at 14,000g at 4°C for 30 minutes.
3. Remove all the supernatant except a small amount (do not touch the bottom with the pipette tip) and resuspend in folding buffer (prepared from the 10x stock + 12.5 mM MgCl2).

6.3.2 Gel electrophoresis protocol

Gel Preparation

1. Weigh 0.75 g of agarose and place it in a >100 mL Erlenmeyer flask.
2. Add 50 mL of 0.5x TAE and swirl to resuspend the agarose powder.
3. Microwave the mixture at high power until it starts boiling. Ensure that all agarose is dissolved. If not, swirl and microwave further until completely dissolved.
4. Let the solution cool for about 30 seconds to a minute under running water or on ice (important: $MgCl_2$ should not be added while boiling).
5. Add 625 μL of 1 M $MgCl_2$ to achieve a final concentration of 12.5 mM. Swirl well to mix.
6. Add the necessary amount of SYBR Safe or EtBr for a final concentration of 1x. Swirl well to mix.
7. Cast the gel in a tray with a comb.

Gel Electrophoresis

1. Gently remove the comb and place the tray with the gel in the gel box. Fill the box with 0.5x TAE containing 12.5 mM $MgCl_2$ until the gel is fully covered.

2. Prepare the samples:

   - Mix 2 μL of the folded origami solution with 1 μL of 6x loading dye and 3 μL of water.
   - Prepare the scaffold sample by mixing 1 μL of 110 nM scaffold with 1 μL of loading dye and 4 μL of water.
   - Prepare the DNA ladder by mixing 1 μL of the ladder (1 kb) with 1 μL of loading dye and 4 μL of water.

3. Load the prepared samples into the wells of the gel.

4. Run the gel at 3 V/cm (approximately 60 V) and 140 mA for about 2 hours. Use an ice bath or place the gel box in a cold room if possible. Replenish the buffer after 1 hour as Mg precipitates out of solution at the cathode as $Mg(OH)_2$.

5. Visualize the gel using a BioRad imager with SYBR Safe setting and auto exposure time.

Bibliography

[1] A. V. Bayles, T. M. Squires, and M. E. Helgeson, "Dark-field differential dynamic microscopy", *Soft Matter*, vol. 12, no. 8, pp. 2440–2452, 2016. DOI: 10.1039/c5sm02576a.

[2] B. J. Berne and R. Pecora, *Dynamic Light Scattering: With Applications to Chemistry, Biology, and Physics* (Dover Books on Physics), New edition. Courier Corporation, 2013, p. 384, ISBN: 0486320243, 9780486320243.

[3] E. Betzig, G. H. Patterson, R. Sougrat, *et al.*, "Imaging intracellular fluorescent proteins at nanometer resolution", *Science*, vol. 313, no. 5793, pp. 1642–1645, 2006. DOI: 10.1126/science.1127344.

[4] M. J. Boyle, Y. E. Goldman, and R. J. Composto, "Enhancing nanoparticle detection in interferometric scattering (iscat) microscopy using a mask r-cnn", eng, *The journal of physical chemistry. B*, vol. 127, no. 16, pp. 3737–3745, 2023, ISSN: 1520-6106.

[5] J. M. Brockman, H. Su, A. T. Blanchard, *et al.*, "Live-cell super-resolved paint imaging of piconewton cellular traction forces", eng, *Nature methods*, vol. 17, no. 10, pp. 1018–1024, 2020, ISSN: 1548-7091.

[6] M. Chalfie, G. Euskirchen, W. Ward, and D. Prasher, "Green fluorescent protein as a marker for gene expression", *Science*, vol. 263, no. 5148, pp. 802–805, 1994. DOI: 10.1126/science.8303295.

[7] C.-Y. Cheng, Y.-H. Liao, and C.-L. Hsieh, "Dynamic signal of live biological cells under interferometric scattering (iscat) microscopy and its impacts on single-particle tracking", *Journal of Physics D: Applied Physics*, vol. 54, no. 36, p. 364 001, 2021. DOI: 10.1088/1361-6463/ac083e.

[8] R. M. Christie, "Fluorescent dyes", in *Handbook of Textile and Industrial Dyeing: Principles, Processes and Types of Dyes*, M. Clark, Ed., Cambridge, UK: Woodhead Publishing, 2011, pp. 562–586.

[9] A. H. Clowsley, W. T. Kaufhold, T. Lutz, *et al.*, "Repeat dna-paint suppresses background and non-specific signals in optical nanoscopy", *Nature Communications*, vol. 12, p. 501, 2021. DOI: 10.1038/s41467-020-20686-z. [Online]. Available: https://doi.org/10.1038/s41467-020-20686-z.

[10] W. T. Corporation, *Dynapro nanostar user's guide*, Version 7.1 (M1400 Rev. K), Wyatt Technology Corporation, Santa Barbara, CA, USA, 2010. [Online]. Available: https://physiology.case.edu/media/eq_manuals/eq_manual_Dynamics_Users_Guide_M1400_Rev_K.pdf.

[11] M. Dahmardeh, H. Mirzaalian Dastjerdi, H. Mazal, H. Köstler, and V. Sandoghdar, "Self-supervised machine learning pushes the sensitivity limit in label-free detection of single proteins below 10 kda", eng, *Nature methods*, vol. 20, no. 3, pp. 442–447, 2023, ISSN: 1548-7091.

[12] H. M. Dastjerdi, M. Dahmardeh, A. Gemeinhardt, R. Gholami Mahmoodabadi, H. Köstler, and V. Sandoghdar, "Optimized analysis for sensitive detection and analysis of single proteins via interferometric scattering microscopy", *Journal of Physics D: Applied Physics*, vol. 55, no. 5, p. 054 002, 2022. DOI: 10.1088/1361-6463/ac2f68.

[13] S. Dey, R. Rivas-Barbosa, F. Sciortino, E. Zaccarelli, and P. Zijlstra, "Biomolecular interactions on densely coated nanoparticles: A single-molecule perspective", *Nanoscale*, vol. 16, no. 9, pp. 4872–4879, 2024. DOI: 10.1039/d3nr06140j.

[14] S. Engel, E.-C. Fritz, and B. J. Ravoo, "New trends in the functionalization of metallic gold: From organosulfur ligands to n-heterocyclic carbenes", *Chemical Society Reviews*, vol. 46, no. 8, pp. 257–275, 2017. DOI: 10.1039/c7cs00023e.

[15] S. Feng and H. G. Winful, "Physical origin of the gouy phase shift", eng, *Optics letters*, vol. 26, no. 8, pp. 485–487, 2001, ISSN: 0146-9592.

[16] M. G. L. Gustafsson and W. W. Webb, "Nonlinear structured-illumination microscopy: Wide-field fluorescence imaging with theoretically unlimited resolution", *Proceedings of the National Academy of Sciences*, vol. 102, no. 37, pp. 13 081–13 086, 2005. DOI: 10.1073/pnas.0406877102.

[17] M. Heilemann, S. van de Linde, M. Schüttpelz, *et al.*, "Subdiffraction-resolution fluorescence imaging with conventional fluorescent probes", *Angewandte Chemie International Edition*, vol. 47, no. 33, pp. 6172–6176, 2008. DOI: 10.1002/anie.200802376.

[18] S. W. Hell and J. Wichmann, "Breaking the diffraction resolution limit by stimulated emission: Stimulated-emission-depletion fluorescence microscopy", eng, *Optics letters*, vol. 19, no. 11, pp. 780–782, 1994, ISSN: 0146-9592.

[19] S. T. Hess, T. P. K. Girirajan, and M. D. Mason, "Ultra-high resolution imaging by fluorescence photoactivation localization microscopy", *Biophysical Journal*, vol. 91, no. 11, pp. 4258–4272, 2006. DOI: 10.1529/biophysj.106.091116.

[20] F. Hitzelhammer, A. Dostálová, I. Zykov, *et al.*, "Unified simulation platform for interference microscopy", *ACS Photonics*, vol. 11, no. 7, pp. 2745–2756, 2024. DOI: 10.1021/acsphotonics.4c00621.

[21] K. Holanová, M. Vala, and M. Piliarik, "[invited] optical imaging and localization of prospective scattering labels smaller than a single protein", *Optics and Laser Technology*, vol. 109, pp. 323–327, 2019. DOI: 10.1016/j.optlastec.2018.08.014.

[22] P. B. Johnson and R. W. Christy, "Optical constants of the noble metals", *Phys. Rev. B*, vol. 6, no. 12, pp. 4370–4379, 1972. DOI: 10.1103/PhysRevB.6.4370.

[23] C. Kielar, Y. Xin, B. Shen, *et al.*, "On the stability of dna origami nanostructures in low-magnesium buffers", *Angewandte Chemie International Edition*, vol. 57, no. 30, pp. 9470–9474, 2018. DOI: 10.1002/anie.201802890.

[24] J. Kwon, M. S. Elgawish, and S. H. Shim, "Bleaching-resistant super-resolution fluorescence microscopy", *Advanced Science*, vol. 9, 2022. DOI: 10.1002/advs.202200000. [Online]. Available: https://onlinelibrary.wiley.com/journal/21983844.

[25] P. P. Laissue, R. A. Alghamdi, P. Tomancak, E. G. Reynaud, and H. Shroff, "Assessing phototoxicity in live fluorescence imaging", eng, *Nature methods*, vol. 14, no. 7, pp. 657–661, 2017, ISSN: 1548-7091.

[26] C. Leduc, S. Si, J. Gautier, *et al.*, "A highly specific gold nanoprobe for live-cell single-molecule imaging", eng, *Nano letters*, vol. 13, no. 4, pp. 1489–1494, 2013, ISSN: 1530-6984.

[27] C. Lin, R. Jungmann, A. M. Leifer, *et al.*, "Submicrometre geometrically encoded fluorescent barcodes self-assembled from dna", eng, *Nature chemistry*, vol. 4, no. 10, pp. 832–839, 2012, ISSN: 1755-4330.

[28] R. Lin, A. H. Clowsley, T. Lutz, D. Baddeley, and C. Soeller, "3d super-resolution microscopy performance and quantitative analysis assessment using dna-paint and dna origami test samples", eng, *Methods (San Diego, Calif.)*, vol. 174, pp. 56–71, 2020, ISSN: 1046-2023.

[29] A. K. R. Lytton-Jean and C. A. Mirkin, "A thermodynamic investigation into the binding properties of dna functionalized gold nanoparticle probes and molecular fluorophore probes", *Journal of the American Chemical Society*, vol. 127, no. 37, pp. 12 754–12 755, 2005. DOI: 10.1021/ja052255o.

[30] M. Mazaheri, K. Kasaian, D. Albrecht, *et al.*, "Iscat microscopy and particle tracking with tailored spatial coherence", *Optica*, vol. 11, no. 7, pp. 1030–1038, Jul. 2024. DOI: 10.1364/OPTICA.523788. [Online]. Available: https://opg.optica.org/optica/abstract.cfm?URI=optica-11-7-1030.

[31] D. J. Nieves, K. Gaus, and M. A. B. Baker, "Dna-based super-resolution microscopy: DNA-PAINT", *Genes*, vol. 9, no. 12, p. 621, 2018. DOI: 10.3390/genes9120621.

[32] L. M. Ostersehlt, D. C. Jans, A. Wittek, *et al.*, "DNA-PAINT MINFLUX nanoscopy", *Nature Methods*, vol. 19, no. 9, pp. 1072–1075, 2022. DOI: 10.1038/s41592-022-01577-1. [Online]. Available: https://doi.org/10.1038/s41592-022-01577-1.

[33] K. Pearce, F. Wang, and P. J. Reece, "Dark-field optical tweezers for nanometrology of metallic nanoparticles", *Optics Express*, vol. 19, no. 25, pp. 25 559–25 569, 2011. DOI: 10.1364/OE.19.025559.

[34] M. Piliarik and V. Sandoghdar, "Direct optical sensing of single unlabelled proteins and super-resolution imaging of their binding sites", *Nature Communications*, vol. 5, no. 1, p. 4495, 2014. DOI: 10.1038/ncomms5495.

[35] B. Platzer, "Analysing supported lipid bilayer dynamics with interferometric scattering microscopy and fluorescence imaging", *Wien*, 2024.

[36] J. Ray and G. S. Manning, "Effect of counterion valence and polymer charge density on the pair potential of two polyions", eng, *Macromolecules*, vol. 30, no. 19, pp. 5739–5744, 1997, ISSN: 0024-9297.

[37] P. W. K. Rothemund, "Folding dna to create nanoscale shapes and patterns", *Nature*, vol. 440, no. 7082, pp. 297–302, 2006. DOI: 10.1038/nature04586.

[38] V. Sandoghdar, A. Renn, P. Kukura, and M. Celebrano, "Single-molecule imaging by optical absorption", *Nature Photonics*, vol. 5, no. 2, pp. 95–98, 2011. DOI: 10.1038/nphoton.2010.290.

[39] J. Schnitzbauer, M. T. Strauss, T. Schlichthaerle, F. Schueder, and R. Jungmann, "Super-resolution microscopy with dna-paint", *Nature Protocols*, vol. 12, no. 6, pp. 1198–1228, 2017. DOI: 10.1038/nprot.2017.024.

[40] F. Schueder, J. Lara-Gutiérrez, B. J. Beliveau, *et al.*, "Multiplexed 3d super-resolution imaging of whole cells using spinning disk confocal microscopy and dna-paint", *Nature Communications*, vol. 8, p. 2090, 2017. DOI: 10.1038/s41467-017-02028-8. [Online]. Available: https://doi.org/10.1038/s41467-017-02028-8.

[41] F. Schueder, J. Stein, F. Stehr, *et al.*, "An order of magnitude faster dna-paint imaging by optimized sequence design and buffer conditions", *Nature Methods*, vol. 16, no. 11, pp. 1101–1104, 2019. DOI: 10.1038/s41592-019-0584-7.

[42] A. Sharonov and R. M. Hochstrasser, "Wide-field subdiffraction imaging by accumulated binding of diffusing probes", *Proc Natl Acad Sci U S A*, vol. 103, no. 50, 17142314, pp. 18 911–18 916, 2006. DOI: 10.1073/pnas.0609643104.

[43] O. Shimomura, F. H. Johnson, and Y. Saiga, "Extraction, purification and properties of aequorin, a bioluminescent protein from the luminous hydromedusan, *Aequorea*", *J. Cell. Comp. Physiol.*, vol. 59, pp. 223–239, 1962. DOI: 10.1002/jcp.1030590302.

[44] J. K. D. Singh, M. T. Luu, A. Abbas, and S. F. J. Wickham, "Switchable DNA-origami nanostructures that respond to their environment and their applications", *Biophysical Reviews*, vol. 10, no. 5, pp. 1283–1293, 2018. DOI: 10.1007/s12551-018-0462-z.

[45] C. K. Spahn, M. Glaesmann, J. B. Grimm, A. X. Ayala, *et al.*, "A toolbox for multiplexed super-resolution imaging of the e. coli nucleoid and membrane using novel paint labels", *Scientific Reports*, vol. 8, 2018. DOI: 10.1038/s41598-018-29545-6. [Online]. Available: https://www.nature.com/articles/s41598-018-29545-6.

[46] S. Spindler, J. Ehrig, H. Stein, and V. Sandoghdar, "High-speed single particle tracking on model lipid membranes", *Biophysical Journal*, vol. 110, no. 3, 649a–649a, 2016. DOI: 10.1016/j.bpj.2015.11.3473.

[47] S. Strauss and R. Jungmann, "Up to 100-fold speed-up and multiplexing in optimized dna-paint", *Nature Methods*, vol. 17, no. 8, pp. 789–791, 2020. DOI: 10.1038/s41592-020-0869-x.

[48] L.-Z. Sun, J.-L. Qian, P. Cai, and X. Xu, "Mutual effects between single-stranded dna conformation and na+-mg2+ ion competition in mixed salt solutions", eng, vol. 24, no. 35, pp. 20 867–20 881, 2022, ISSN: 1463-9076.

[49] R. W. Taylor and V. Sandoghdar, "Interferometric scattering (iscat) microscopy & related techniques", *arXiv preprint arXiv:1812.10765*, 2018. DOI: 10.48550/arxiv.1812.10765.

[50] R. W. Taylor and V. Sandoghdar, "Interferometric scattering microscopy: Seeing single nanoparticles and molecules via rayleigh scattering", *Nano Letters*, vol. 19, no. 8, pp. 4827–4835, 2019. DOI: 10.1021/acs.nanolett.9b01822.

[51] W. Thielicke and E. J. Stamhuis, "Pivlab – towards user-friendly, affordable and accurate digital particle image velocimetry in matlab", *Journal of Open Research Software*, vol. 2, Oct. 2014. DOI: 10.5334/jors.bl.

[52] M. Zacchia, M. L. Abategiovanni, S. Stratigis, and G. Capasso, "Potassium: From physiology to clinical implications", *Kidney Diseases (Basel)*, vol. 2, no. 2, pp. 72–79, Jun. 2016, Epub 2016 May 26. DOI: 10.1159/000446268.

[53] J. Zähringer, F. Cole, J. Bohlen, F. Steiner, I. Kaminska, and P. Tinnefeld, "Combining pMINFLUX, graphene energy transfer and DNA-PAINT for nanometer precise 3D super-resolution microscopy", *Light: Science & Applications*, vol. 12, no. 1, 2023. DOI: 10.1038/s41377-023-01111-8. [Online]. Available: https://doi.org/10.1038/s41377-023-01111-8.

[54] K. Žambochová, I.-B. Lee, J.-S. Park, S.-C. Hong, and M. Cho, "Axial profiling of interferometric scattering enables an accurate determination of nanoparticle size", *Optics Express*, vol. 31, pp. 10 101–10 113, 2023.

[55] X. Zhuang, M. J. Rust, and M. Bates, "Sub-diffraction-limit imaging by stochastic optical reconstruction microscopy (storm)", *Nature Methods*, vol. 3, no. 10, pp. 793–796, 2006. DOI: 10.1038/nmeth929.